

Received March 30, 2021; revised June 11, 2021; accepted June 30, 2021; date of publication July 13, 2021;  
date of current version August 12, 2021.

Digital Object Identifier 10.1109/TQE.2021.3096480

# Engineering the Quantum Scientific Computing Open User Testbed

SUSAN M. CLARK<sup>1</sup>, DANIEL LOBSER<sup>1</sup>, MELISSA C. REVELLE<sup>1</sup>,  
 CHRISTOPHER G. YALE<sup>1</sup>, DAVID BOSSERT<sup>1</sup>, ASHLYN D. BURCH<sup>1</sup>,  
 MATTHEW N. CHOW<sup>1,2,3</sup>, CRAIG W. HOGLE<sup>1</sup>, MEGAN IVORY<sup>1</sup>, JESSICA PEHR<sup>4</sup>,  
 BRADLEY SALZBRENNER<sup>1</sup>, DANIEL STICK<sup>1</sup>, WILLIAM SWEATT<sup>1</sup>,  
 JOSHUA M. WILSON<sup>1</sup>, EDWARD WINROW<sup>1</sup>, AND PETER MAUNZ<sup>4</sup>

<sup>1</sup>Sandia National Laboratories, Albuquerque, NM 87123 USA

<sup>2</sup>Department of Physics and Astronomy, University of New Mexico, Albuquerque, NM 87131 USA

<sup>3</sup>Center for Quantum Information and Control, University of New Mexico, Albuquerque, NM 87131 USA

<sup>4</sup>IonQ, Inc., College Park, MD 20740 USA

Corresponding author: Susan M. Clark (sclark@sandia.gov).

This work was supported in part by the U.S. Department of Energy, Office of Science, Office of Advanced Scientific Computing Research Quantum Testbed Program and in part by Sandia National Laboratories' Directed Research and Development Program. Sandia National Laboratories is a multimission laboratory managed and operated by National Technology and Engineering Solutions of Sandia, LLC, a wholly owned subsidiary of Honeywell International Inc., for the U.S. Department of Energy's National Nuclear Security Administration under Contract DE-NA0003525.

**ABSTRACT** The Quantum Scientific Computing Open User Testbed (QSCOUT) at Sandia National Laboratories is a trapped-ion qubit system designed to evaluate the potential of near-term quantum hardware in scientific computing applications for the U.S. Department of Energy and its Advanced Scientific Computing Research program. Similar to commercially available platforms, it offers quantum hardware that researchers can use to perform quantum algorithms, investigate noise properties unique to quantum systems, and test novel ideas that will be useful for larger and more powerful systems in the future. However, unlike most other quantum computing testbeds, the QSCOUT allows both quantum circuit and low-level pulse control access to study new modes of programming and optimization. The purpose of this article is to provide users and the general community with details of the QSCOUT hardware and its interface, enabling them to take maximum advantage of its capabilities.

**INDEX TERMS** Laser excitation, laser mode locking, quantum entanglement, vacuum technology.

## I. OVERVIEW AND SYSTEM DESIGN

Experimental quantum computing is beginning to realize its potential for computational speedup through recent demonstrations of specialized algorithms with as few as 50 qubits [1], [2]. These machines are considered noisy intermediate-scale quantum (NISQ) computers [3], and though their ability to solve relevant real-world problems is limited by their size and fidelity, they are very useful for investigating the best way to build and operate a future fault-tolerant quantum computer. While access to NISQ hardware has become available over the past few years [4]–[6], it is still scarce and highly constrained to a small set of fixed physical operations. We have developed the Quantum Scientific Computing Open User Testbed (QSCOUT) platform to reduce these two barriers in order to accelerate progress by the scientific community.

QSCOUT's user program begins with a call for proposals, where the details of the upcoming system are described. Up-to-date information about proposal calls and current capabilities is available on the website: <https://qscout.sandia.gov>. Proposals are reviewed by a committee external to the QSCOUT program and judged on their scientific merit and feasibility given the capabilities of the current system. Selected proposals are guaranteed run time on the machine as well as access to QSCOUT scientists if desired, for collaboration. Additionally, complete specifications of the system can be provided for each algorithm run, including, but not limited to, pulse lengths and secular frequencies. Other specifications requested by the user can also be provided. There is no fee to use the QSCOUT system.

The QSCOUT platform consists of a small number of  $^{171}\text{Yb}^+$  ion qubits. The first round of user

experiments has two to three ions, with plans to expand to a linear chain of 32 ions in later rounds. Trapped ions have long coherence times [7], [8], high gate fidelities [9], and very low state preparation and measurement (SPAM) errors [10], making them an ideal system to build a quantum processor. The targets for the QSCOUT are to provide up to 32 qubits with >99.5% fidelity single-qubit gates, >98% fidelity two-qubit gates, and <0.5% crosstalk. Currently, we consistently observe >95% fidelity two-qubit gates, limiting circuit depth to  $\approx 10$  two-qubit gates. Despite being arranged in a linear chain, the qubits are fully connected through the vibrational modes of the chain, meaning a two-qubit gate can occur between any pair of ions [11] in the chain without dedicated SWAP gates or physical swapping [12]. Single-qubit and two-qubit gates are performed using a pulsed laser to excite Raman transitions between the hyperfine states of the qubit. In order to individually address the ions, one path of the pulsed-laser beam is split into 32 beams, with each beam passing through a distinct channel of a multichannel acoustooptic modulator (AOM) before being focused onto a single ion. This arrangement allows for independent frequency, amplitude, and phase control of the laser pulses applied to each ion.

To trap a linear chain of ions, we are using a high optical access (HOA-2.1) surface trap fabricated at Sandia National Laboratories [13], because it is capable of precisely controlling ion spacing and manipulating chains of ions. Additionally, it has demonstrated heating rates above the slotted portion of the trap in the range of 100–200 quanta/s [14] at the radial secular frequencies used in QSCOUT experiments (see Table 6). To maintain a linear chain for enough time to perform many quantum operations, the trap must be under ultra-high vacuum (UHV) to limit collisions that “melt” the ion crystal or eject ions from the trap. The vacuum chamber must have windows for optical access as well as electrical feedthroughs for radio frequency (rf) and dc voltages to reach the trap. The details of the vacuum chamber are described in Section II. Section III discusses the specific laser frequencies and locks needed for trapping, cooling, and detecting  $^{171}\text{Yb}^+$  ions, as well as our optomechanical system for minimizing vibrations and drift that degrade the quality of the delivered light. Quantum gates are performed using a 355-nm pulse train [15], which has tight spatial tolerances to achieve individual addressing of closely spaced ions. Our technique for pulse train spacing compensation and optical delivery is outlined in Section IV. Distinguishable detection of ions is achieved by imaging light from each ion into a separate core of a multimode fiber array, with each core coupled to its own photomultiplier tube (PMT) for counting photons. Section V describes this detection method in more detail. We also developed new electrical hardware to control the timing, frequency, and amplitude of the rf pulses needed to modulate the optical signals that are delivered to the ions. This device and corresponding firmware are described in Section VI. The high-level programming language for users to interface with our hardware, Jaqal, has been described in [16], and design

decisions described in [17]. In Section VII, we describe the resulting ion performance achieved in preparation for the first round of user experiments, and finally, in Section IX, we provide full specifications of the QSCOUT system.

## II. UHV CHAMBER

Because the QSCOUT relies on the realization of multi-ion chains, the background gas pressure in the system is of paramount importance. While an individual ion lifetime in a surface-electrode trap is typically hours-long (even a few days), as we scale up to larger chains, the chain lifetime reduces as more ions are subject to background gas collisions [18]. Since most collisions at room temperature are of sufficient energy to destabilize the ion chain, limiting collisions results in fewer ion losses, fewer quantum algorithm restarts, and faster processing time. To this end, we develop a UHV system intended to realize long-lived ion chains incorporating vacuum practices from other fields to achieve lower background pressure.

UHV has been a standard of vacuum technology for decades. It has relied on the use of stainless steel components, copper gasketing, limiting organics to low-outgassing plastics, welding and brazing of components such as viewports, and utilizing ion pumps to maintain the necessary vacuum pressure. Additionally, a vacuum bake is a standard procedure to remove water vapor and other outgassing residues from the internal environment.

In trapped-ion systems, the vacuum chamber must support an ion trap, an ion source, and have viewports for laser access. In our chamber, the central experimental region is a Kimball Physics 6-in CF (ConFlat flange) Spherical Square (see Fig. 1). A feedthrough flange containing electrical and rf connections is attached at the top of the chamber. A stainless steel platform anchored to the feedthrough is suspended inside the chamber. The platform and its various components are all machined from Grade 316L stainless steel and electropolished. The microfabricated surface-electrode ion trap is attached to this platform, facing downward to make it less likely dust particles will attach to the surface [see Fig. 2(a)]. The trap uses an rf signal on a single large electrode to generate the radial trapping pseudopotential, as well as a number of smaller dc electrodes to shape the potential and confine the ion to a particular region of the trap [13], [19], [20]. A thermal oven is used to create a neutral Yb flux, which is then photoionized to generate ions for trapping (more details are provided in Section III-A). Imaging is performed from the bottom of the chamber and utilizes a re-entrant viewport to allow for the small working distance of the imaging lens assembly (more details are given in Section V). The spherical square has an octagonal structure, and viewports are affixed to seven of the eight sides to optically access the trap. One of the viewports that allow for optical access perpendicular to the trap axis is also a re-entrant viewport, visible in Fig. 1. This is needed for individual ion addressing using lasers, described in Section IV. The transition to the pumping region of the chamber consists of a stainless steel vacuum cross and

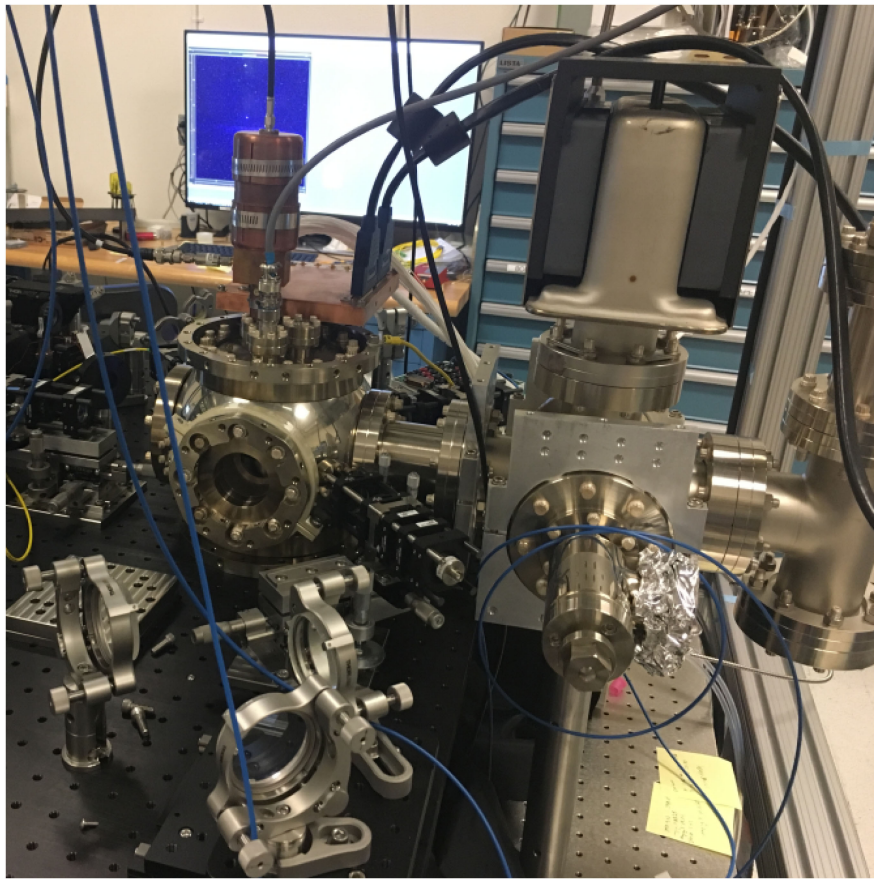


**FIGURE 1.** UHV chamber for trapped ion quantum operations. The chamber consists of an experimental region (left) and a pumping region (right). The chamber has rf and dc feedthroughs that support trap potential generation as well as viewports for laser addressing of the ions.

tee. This supports a 50-L/s ion pump (Agilent Varian VacIon Plus 55 StarCell), an ion gauge (Agilent Varian UHV-24P Nude Bayard-Alpert Ion Gauge with dual Ir-Th filament), a titanium sublimation pump (TSP), and all-metal bakeable valve. To prevent titanium film from sputtering on the trap surface, the TSP is positioned out of direct line of sight from the trap. For convenience, we constructed two chambers so that the backup, already baked with a trap, can be swapped as needed.

#### A. REQUIREMENTS

The dc and rf wiring that convey the voltages for trap generation traditionally use organic materials in the form of insulation, multipin connectors, and circuit boards. The materials include polyether ether ketone (PEEK), polyimide films such as Kapton (DuPont), and RO4350B (Rogers Corporation). While these materials are typically classified as low-outgassing materials (total mass loss <1%) [21], they can still contribute to the background gas pressure present in the chamber. In addition, the bulk of the chamber is manufactured from Grade 304 and 316 stainless steel; however, stainless steel is susceptible to hydrogen diffusion and adsorption [22], [23], which also contributes hydrogen to the overall background pressure. In the QSCOUT chambers, we

focused on eliminating these organics and reducing hydrogen within the stainless steel in an effort to improve our vacuum pressure.

#### B. HYDROGEN MITIGATION

In an effort to decrease the amount of hydrogen within the stainless steel components, we subject all of the purely stainless steel components to a high-temperature bake process. This includes the trap platform, the experimental chamber, and all of the nipples, tees, crosses, adapters, and blanks. Prior to baking, the parts are cleaned with solvents and degreasers that include 3M Novec 72DE, acetone, and isopropanol. Initially, they are baked in a dry H<sub>2</sub> atmosphere at 1000 °C for 30–45 min to remove any organic material from the stainless steel. Afterward, the parts are baked in a vacuum environment for 4 h at 800 °C to remove hydrogen adsorbed and diffused into the steel [23], [24].

The stainless steel elements of other components, such as viewports and feedthrough flanges, were subjected to a vacuum bake at 800 °C for 10 h by the manufacturer (MPF Inc.) prior to assembly with the feedthrough components or windows. Other elements including the ion pump, TSP, ion gauge, and bakeable valve were unable to be subjected to any aggressive bake process due to inherent elements that might

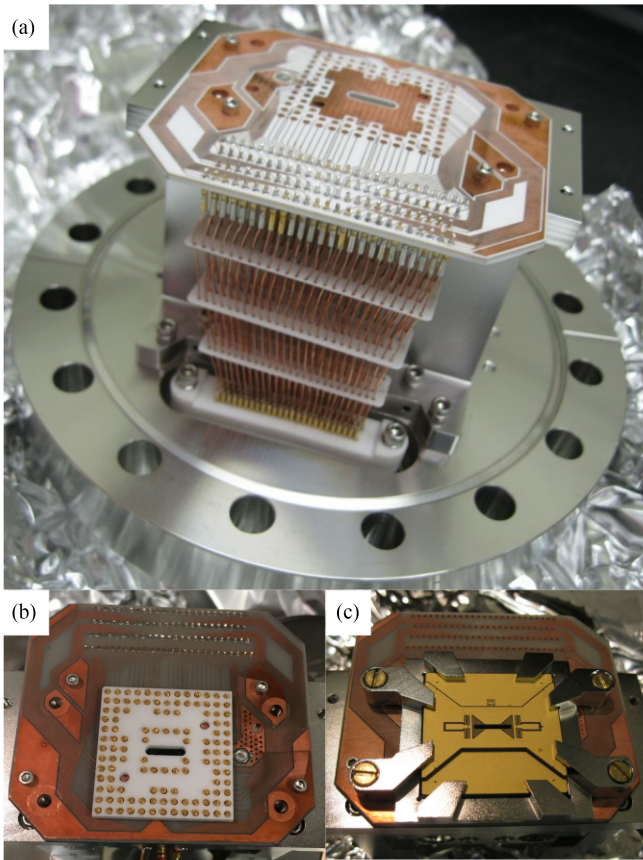


**FIGURE 2.** (a) Trap platform attached to the feedthrough flange. The trap platform, on which the trap will be mounted, is machined from stainless steel. The dc signals are routed via bare copper wires from a Micro-D feedthrough to an  $\text{Al}_2\text{O}_3$  ceramic signal routing board. These wires are separated with  $\text{Al}_2\text{O}_3$  spacers to prevent shorting. (b) Signal routing board is a ceramic (AlN pictured here) circuit board with bare copper traces. A MACOR spacer is placed on top of the board with a series of FuzzButtons placed inside to provide electrical contact with the trap package. (c) Trap is secured to the board and ceramic spacer with a stainless steel clamp that preserves optical access to the ions.

be detrimentally affected (copper, filaments of tungsten, thoriated iridium, or titanium).

After assembling the chamber, we bake it without the trap for several weeks at 200 °C. After the bake, we slowly vent (over the course of several hours) to minimize particle disturbance in the trap. Within 48 h of completing the bake, we install the trap into the chamber in a cleanroom environment. Then, a final bake is performed for five to seven days at 200 °C. The second bake is limited to a shorter time to prevent the accumulation of Al–Au intermetallics at the site of our wirebonds (i.e., purple plague) [13], [25], [26]. As the final step, we fire the TSP every 32 h until the pressure as measured on the ion gauge does not improve at all with further firings of the TSP, usually after five to seven days.

### C. ELIMINATION OF ORGANICS

For every element in the system in which the typical component contains organic material, we developed a suitable

replacement using ceramic materials, such as the machinable ceramic MACOR (Corning), aluminum nitride (AlN), and aluminum oxide ( $\text{Al}_2\text{O}_3$ ). Due to the brittleness of ceramic materials, additional design modifications were implemented to eliminate potential stresses on these ceramics. Each of these elements is described as follows.

#### 1) DC DELIVERY

To bring the 100 dc signals to the trap control electrodes, we use a 100-pin Micro-D vacuum feedthrough. The standard commercial connector for this feedthrough on the vacuum side consists of a PEEK connector with 100 Kapton coated wires. Instead, we use a MACOR version of the connector (Winchester Interconnect) and a series of bare oxygen-free high-conductivity (OFHC) copper wires (AWG28) soldered into the receptacle pins of the connector. These wires are  $\approx 2$  in long and are connected to the trap platform for distribution to the trap package, as shown in Fig. 2(a). The pitch of Micro-D pins is 0.05 in with a row spacing of 0.043 in, each row offset by 0.025 in. We fan out the wires to a pitch of 0.07 in with 0.16-in row spacing and 0.035-in row offset. In addition, to prevent shorting, we use three 0.05-in-thick  $\text{Al}_2\text{O}_3$  spacers (laser machined with holes and grooves) to support and aid the separation of wires. The spacers remain solidly in place due to the tension of the wires. At the top of the trap platform sits a ceramic circuit board for signal delivery. Due to the high thermal conductivity of ceramic, the bare wires cannot be soldered directly to the board. Instead, BeCu pins are soldered directly to the board via a solder reflow oven process, using SAC305 (96.5% Sn, 3% Ag, and 0.5% Cu) solder. The BeCu pins are #23 crimp contact pins (Glenair), without any markings, and are typically used in circular MIL spec connectors. The pins are small and thin enough to provide enough thermal isolation that the wires can be directly hand-soldered to the pins with SAC305 solder. All water-soluble flux from the solder is cleaned off through water baths, and then, the entire assembly is cleaned with a series of ultrasonic baths with solvents and degreasers, discussed in Section II-B.

#### 2) SIGNAL DELIVERY CIRCUIT BOARD

The circuit board, manufactured by Millennium Circuits, consists of a 0.059-in-thick substrate of an aluminum-based ceramic. The first chamber built was outfitted with an AlN circuit board [see Fig. 2(b)], while the second has a  $\text{Al}_2\text{O}_3$  board [see Fig. 2(a)]. The variation between the two chambers was part of an effort to reduce the board's thermal conductivity and allow for direct soldering of the wires to the board, but in the end, both board materials require the intermediate step of BeCu pins soldered via reflow. These substrates contain bare copper traces on the top for signal routing and a copper ground plane on the bottom, with the copper thickness corresponding to 1 oz./1 ft<sup>2</sup>. Because the board is intended for a UHV environment, it contains no soldermask, no silkscreen, nor any other finish. The traces on

the top of board are 0.005 in thick and route the signal from the 100 dc wires to pads on the center of the board. These pads correspond to pads on the bottom of the trap package. In addition, the board contains routing for the trap rf. A thick AWG11 OFHC copper wire is soldered to the board (also via a solder reflow oven process) to carry the  $\approx 50$  MHz signal. The rf delivery is discussed in Section II-C4. The board also contains a series of holes for mounting to the trap platform inside the chamber, which are all copper plated to improve ground connection. The chamber itself acts as ground for both the rf and dc signals.

### 3) TRAP MOUNTING

Our trap package consists of a microfabricated surface-electrode trap attached to a ceramic package. For future iterations, we plan to use a trap that is attached via a solder process described in [20] as part of the effort to remove all organics. However, the trap currently in the system is attached to its package with an epoxy.

Our package for these traps previously consisted of a 104-pin grid array (PGA), which contained Kovar pins that are then inserted into a zero-insertion-force (ZIF) socket, which is typically manufactured from PEEK. While the ZIF socket could potentially be manufactured out of a machinable ceramic such as MACOR, there was concern that the insertion and removal of traps may be hampered by brittleness of the ceramic with potential damage to the trap and the socket. As such, we replaced the PGA package with a land grid array package consisting of gold-coated pads on the backside of the package.

The trap is then placed on a machined MACOR spacer. The 0.1-in-thick spacer sits on the circuit board and consists of an array of holes matching up with the array of pads, as well as additional holes for ground connections in the center of the package. Gold-plated beryllium copper 0.12-in-long FuzzButtons (Custom Interconnects) are inserted into each slot in the MACOR spacer [see Fig. 2(b)]. The FuzzButtons provide both the path for the signal (or ground) and the elasticity necessary to ensure contact. In addition, the FuzzButtons eliminate the use of the magnetic Kovar pins found on the PGA packages, thus eliminating a potential source of stray magnetic fields near the ion. The trap is placed on top of the MACOR spacer and FuzzButtons, and a custom clamp machined from 316L stainless steel pushes down on the trap to ensure contact. The clamp is designed to ensure that there is no loss of optical access around the trap. It consists of a series of fingers, which clamp onto the package outside of designed laser path [see Fig. 2(c)].

### 4) TRAP RF DELIVERY

The rf is delivered to the circuit board via an AWG11 bare OFHC copper wire. This rf wire is connected through a barrel connector to another similarly gauged wire affixed to a feedthrough. The chamber serves as the rf ground. The air side of the feedthrough also consists of a ground shield

around the extruding wire, with an air gap (custom MPF P/N A19619-1). A helical resonator can be attached to the air side [27].

Given that the qubit splitting in  $^{171}\text{Yb}^+$  is 12.642 GHz, it is not feasible to drive the qubit transition using an internal microwave antenna, as any signal would be attenuated drastically without the use of an internal coaxial cable. Because of our restriction on the use of organics inside the chamber, we instead use an external microwave horn to drive transitions.

### D. CHARACTERIZATION OF VACUUM

We utilize a variety of measurements to characterize our background pressure. The most rudimentary approach, and least informative, is a measurement of the pressure via the ion gauge, as the reading varies considerably based on the controller used and its particular calibration. Additionally, the ion gauge may underestimate the vacuum pressure since it is calibrated to the nitrogen ionization rate, which is larger than that of helium and hydrogen [28]. The two assembled chambers measured pressures of  $6\text{-}12$  and  $4\text{-}12$  Torr via their respective ion gauges, but with the same controller. We measure pressures using this controller in other chambers used by our group that do not undergo the organic elimination or the hydrogen mitigation. We find that our QSCOUT chambers outperform the others by factors of 2–5.

Another method we use to examine the background pressure is through background gas–ion collision measurements using a double-well potential [29]. We generate a series of double-well trapping potentials with a variable height barrier [see Fig. 3(a)]. Because hydrogen is the dominant residual gas, we begin with a low enough energy barrier to capture a significant portion of all collisions,  $60 \mu\text{eV}$  [29]. The imaging system is intentionally misaligned such that one site appears brighter in the detector than the other. We apply dc voltages to our segmented electrodes to create a shimming field along the trap axis ( $x$ -axis) that can push the ion from one site to the other. The optimal shim field is set in between the values of the shim fields, which cause the ion to occupy each site.

We monitor the number of distinct jumps that occur at several different barrier heights. At each height, we wait for at least 6 h or 20 distinct jumps before increasing the barrier. Fig. 3(b) is a typical response over one 6-h time window. For each potential, we count the number of jumps a single ion makes between the two sites and estimate the collision rate as twice the observed jump rate to account for collisions in which the ion returned to its original site [18], [29]. This collision rate corresponds to all background gas collisions with the ion that have a kinetic energy along the trap axis that is greater than the barrier height. By raising the barrier height, we aim to understand more about the residual gas species remaining in the chamber. Using a Langevin collision model, we estimate partial pressures of these gases [18]. These pressures may be underestimations since the ion jumps are most sensitive to collisions along the trap axis, and off-axis collisions may not result in an ion jump. As we increase the

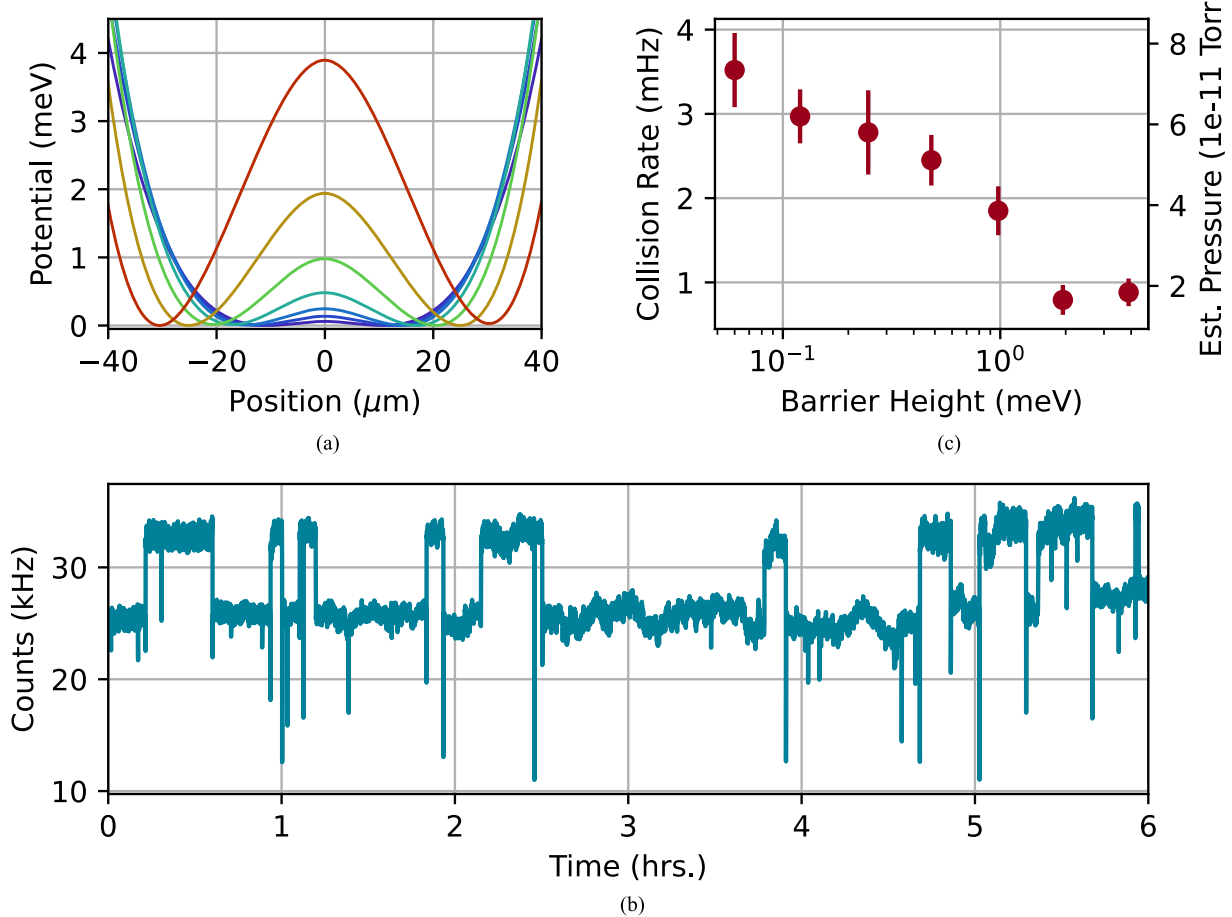


**FIGURE 3.** (a) Series of slices of the axial potentials used to probe background gas collisions. The central barrier can be increased up to  $\approx 4$  meV before reaching voltage limits on the trap dc electrodes (10 V). At each barrier height, we monitor the ion and measure how many times it shifts between the two sites of the potential. (b) Example of the collisions at a  $979\text{-}\mu\text{eV}$  energy barrier. Each scan was taken for at least 6 h. One site registers  $\approx 32$  kHz in the PMT, while the other registers  $\approx 25$  kHz, so hops are visible as changes in received photon counts. (c) Collision rate as a function of barrier height. The collision rate (left axis) can be transformed into an estimated partial pressure (right axis), which assumes that all collisions are with a specific species, in this case hydrogen. The error bars reflect the standard Poissonian counting error. This figure is not to show that the estimated pressure of colliding particles above a particular energy falls off quickly with increasing barrier heights, suggesting that hydrogen is the dominant contributor to collisions.

barrier height, the number of collisions decreases until it flattens out around 2 meV [see Fig. 3(c)]. This behavior suggests that the collisions are dominated by hydrogen, but there are some residual collisions at higher energies. Typically (90% of instances), during experimental runs with chains of ions, a collision will destroy the entire chain. A small fraction of the time, a single ion will go dark, but the chain will remain roughly intact. Regardless of that, the pressure suggested by these collisions is suitable for the purposes of this experiment and shows an improvement of a factor of roughly 2 over other chambers in our group.

### III. CONTINUOUS-WAVE LASER DELIVERY

The  $^{171}\text{Yb}^+$  ion is one of the predominant ion qubits due to its magnetically insensitive hyperfine states for ultrastable qubit transitions [7], relatively simple hyperfine structure (nuclear magnetic spin  $I = 1/2$ ), and optical transitions requiring trapping and cooling lasers in the near-visible UV.

Our scheme for cooling, optical pumping, and detection is very similar to a scheme outlined previously [30]. This section will describe the continuous-wave (cw) lasers needed for trapping and cooling  $^{171}\text{Yb}^+$ , as well as our method for light delivery into the vacuum chamber.

#### A. LEVEL DIAGRAM AND REQUIRED LASERS

We load ions into our trap via a two-photon transition of neutral Yb atoms sublimated from a heated source of solid Yb. The two-photon transition first requires a resonant 399-nm photon, which (with isotope selectively) drives the atom into an excited state. If this excitation is followed by another high-frequency photon ( $\lambda < 394$  nm), the second photon can strip off an electron, resulting in  $^{171}\text{Yb}^+$  [31]. Once Yb is ionized, the pseudopotential created by the combination of rf and dc electric fields from the surface trap will localize it above the chip surface.

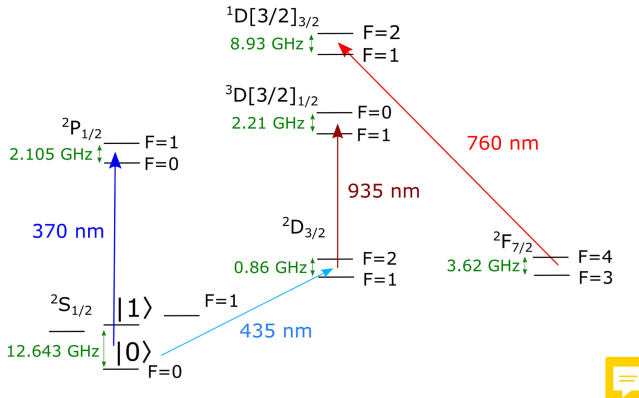


**FIGURE 4.** Energy-level diagram of  $^{171}\text{Yb}^+$  (not to scale) showing lasers used to drive transitions and to keep the ion in the qubit manifold (solid arrows). The magnetic sublevels are shown only for the  $^2\text{S}_{1/2}$  state and the qubit energy levels (labeled  $|0\rangle$  and  $|1\rangle$ ) are identified. The 370-nm laser is the laser used for Doppler cooling, detection, and state preparation (see Fig. 5). The 935-nm laser is used to pump ions out of the  $^2\text{D}_{3/2}$  state, while the 760-nm laser can pump out of the  $^2\text{F}_{7/2}$  state. The 435-nm laser can be used for diagnostics, sideband cooling, or perhaps sympathetic cooling.

The lasers needed to keep the ion in the qubit subspace [ $^2\text{S}_{1/2} |F = 0, m_F = 0\rangle$  ( $|0\rangle$  or “dark”) and  $^2\text{S}_{1/2} |F = 1, m_F = 0\rangle$  ( $|1\rangle$  or “bright”)] are shown in Fig. 4 [30]. Incoherent state manipulation (cooling, detection, and state preparation) uses 370-nm light to excite transitions between the  $^2\text{S}_{1/2} F = 1$  and the  $^2\text{P}_{1/2} F = 0$  states (with sidebands as described below for specific hyperfine state manipulation). The 370-nm light performs Doppler cooling by removing energy through a series of photon absorptions and emissions. Since the pseudopotential supplies a restoring force in all three dimensions, only a single laser is needed to cool the ion; however, to do so, the propagation direction ( $\mathbf{k}$ -vector) must have a projection along each axis of the ion’s secular motion (axial and two radial directions). The polarization needs to be a combination of linear ( $\pi$ ) and both circular ( $\sigma^+$  and  $\sigma^-$ ) directions in order to excite all the necessary transitions. Additionally, the light is red detuned from the resonant transition energy for optimal cooling [30].

During Doppler cooling, 14.7-GHz sidebands are added to the 370-nm beam via a Qubig free-space electrooptic modulator (EOM) to prevent the ion from becoming trapped in  $^2\text{S}_{1/2} F = 0$  hyperfine state, which can happen via off-resonant coupling to the  $^2\text{P}_{1/2} F = 1$  states [see Fig. 5(a)]. On the other hand, to prepare a single ion state, we remove the 14.7-GHz sidebands and add 2.105-GHz sidebands. These sidebands excite to the  $^2\text{P}_{1/2} F = 1$  state from the  $^2\text{S}_{1/2} F = 1$  states, which can spontaneously emit to the  $^2\text{S}_{1/2} F = 0$  state and become trapped there, as shown in Fig. 5(b).

Finally, the 370-nm laser is also used for state detection, as shown in Fig. 5(c). For state detection, in order to keep the ion in a cycling transition between the  $^2\text{S}_{1/2} F = 1$  and  $^2\text{P}_{1/2} F = 0$  states, no sidebands are used on the 370-nm beam. Off-resonant coupling of the ion in the  $^2\text{S}_{1/2} F = 1$

**TABLE 1.** Lasers, Necessary Modulations, and Required Linewidths for Reliable Trapping, State Preparation, and Detection of  $^{171}\text{Yb}^+$

Laser	Linewidth	Cool	Optical Pump	Detect	355 Experiment
370 nm	1 MHz	+ 14.7 GHz	+ 2.105 GHz	On	Off
935 nm	5 MHz	+ 3.07 GHz	+ 3.07 GHz	+ 3.07 GHz	+ 3.07 GHz
760 nm	5 MHz	+ 5.2 GHz	+ 5.2 GHz	+ 5.2 GHz	+ 5.2 GHz

state to the  $^2\text{P}_{1/2} F = 1$  state, which can result in an ion becoming dark if it was bright, is the leading source of detection error and varies depending on optical collection efficiency, detection time, and detection laser power [10], [30]. More rarely, there is off-resonant coupling causing a dark ion to become bright, which also contributes to detection error (see Section V for a more detailed discussion of detection error).

The 370-nm light alone is not sufficient to prevent the ion from decaying into nonqubit states. In particular, from the  $^2\text{P}_{1/2}$  levels, the ion relaxes to the low-lying  $^2\text{D}_{3/2}$  with a branching ratio of 0.5% [30]. To mitigate leakage into this state, we use a 935-nm laser to resonantly excite the ion to the  $^3\text{D}_{[3/2]_{1/2}}$  state, where it then decays back to the  $^2\text{S}_{1/2}$  manifold [32]. During optical pumping, it is necessary to add 3.07-GHz sidebands to the 935-nm laser via a fiber EOM to ensure that the ion is also pumped out of the  $F = 2$  state of the  $^2\text{D}_{3/2}$  manifold. These sidebands are left on during cooling and detection.

Collisions can cause the ion to relax to the  $^2\text{F}_{7/2}$  manifold, which has a lifetime of 3700 days [33]. A 760-nm laser is applied in order to pump out of the  $F$  state by exciting the ion to the  $^1\text{D}_{[3/2]_{1/2}}$  state. From there, it can decay back to the  $S$  manifold [34], [35]. This repumping technique has yet to be tested on the QSCOUT system.

Finally, another laser that is used for characterization of our system is the 435-nm laser. It is used to perform transitions between the  $^2\text{S}_{1/2}$  state and the  $^2\text{D}_{3/2}$  state (as shown in Fig. 4). This is a useful diagnostic tool, especially for sideband cooling of the axial modes (which are not easily accessible via the 355-nm pulsed laser; see Section IV) or for potential sympathetic cooling by using cotrapped non- $^{171}\text{Yb}^+$  isotopes [36]. The 435-nm laser has not yet been used extensively for the QSCOUT, but we have designed to add this capability later.

In summary, Table 1 lists the cw lasers used with  $^{171}\text{Yb}^+$  and the sidebands applied for various stages of ion initialization and readout. The 399-, 935-, and 760-nm lasers are part of the Toptica MDL-PRO rack mountable system. Fibers route light from these lasers to the experiment.

## B. 370-NM LASER PATH

The 370-nm laser is the most complicated in terms of locking, modulation, and delivery requirements. The light needs to be referenced to an atomic source and have a linewidth narrow enough (<1 MHz) to efficiently excite the ion. To meet these requirements, we have a multistep approach consisting of four main modules: the transfer cavity, the laser breakout board with beat-note lock, the modulation board, and beam delivery to the experiment.

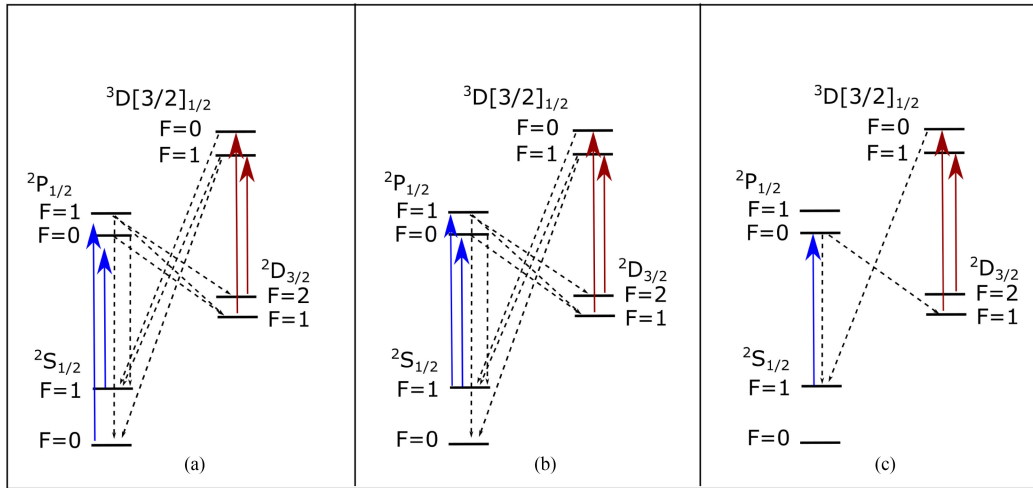


**FIGURE 5.** Applied 370-nm light and sidebands for cooling, optical pumping, and detection (solid blue arrows). Also shown are ion relaxation channels (black dotted lines) and applied 935-nm tones (red solid arrows). (a) For cooling, the 370-nm light is detuned  $-13$  MHz from the resonant transition (transition linewidth,  $\Gamma = 19.7$  MHz) and 14.7-GHz sidebands are added to prevent the ion from becoming trapped in the  $^2S_{1/2}$   $F = 0$  state. (b) For optical pumping, 2.105-GHz sidebands are applied, resulting in the ion becoming trapped in the  $^2S_{1/2}$   $F = 0$  state after several cycles. (c) For detection, sidebands on the 370-nm light are removed, causing the ion to emit many photons, while the light is applied if it is in the  $F = 1$  (bright) state and none if in the  $F = 0$  (dark) state.

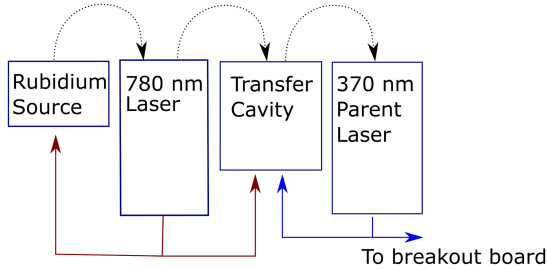


**FIGURE 6.** Schematic of the transfer cavity module. Red and Blue (solid) arrows represent optical connections and dotted black lines represent electrical feedback signals.

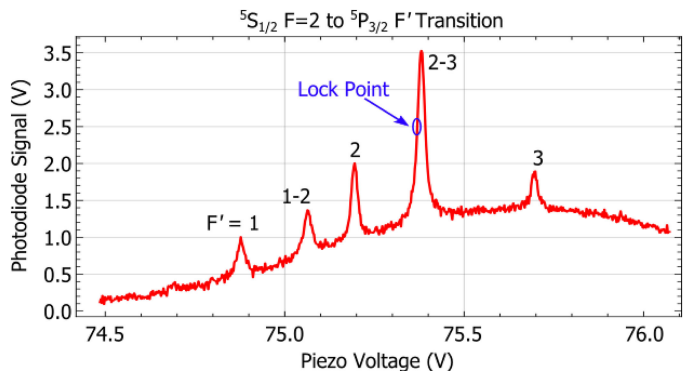


**FIGURE 7.** Doppler free spectrum of  $^{87}\text{Rb}$  used to lock the 780-nm laser.

## 1) TRANSFER CAVITY MODULE

The transfer cavity lock module consists of three separate locks. All three objects being locked (two lasers and a transfer cavity) are mounted on a minus-K 100BM-8 benchtop vibration isolation system inside a Herzan acoustic enclosure to protect them from acoustic noise and provide passive temperature stability.

A schematic of the transfer cavity locking system is shown in Fig. 6. The Toptica DLC Pro 780-nm laser is first locked to a stable Rubidium source. We use a side of fringe lock on the lower frequency side of the  $^5S_{1/2}$   $|F = 2\rangle$  to the  $^5P_{3/2}$   $|F' = 2, m_F = 2-3\rangle$  crossover transition in  $^{87}\text{Rb}$ , due to its relative height and peak sharpness as shown in Fig. 7. The Rubidium source is a Toptica CoSy saturation spectroscopy module with a 5-MHz bandwidth. A Toptica DLC-PRO Lock provides the feedback.

The stabilized light from the 780-nm laser is used to lock an SLS-PZT cavity from Stable Laser Systems. The mirror substrates were coated by FiveNine Optics, Inc., to have a finesse of 1000–3000 for 370 and 780 nm; the cavity length

is scanned with a piezo. We use a standard Pound–Drever–Hall (PDH) technique [37], [38] to lock the cavity by adding  $\sim 16.0$ -MHz sidebands (plus a 3.508-GHz offset for the light to match the cavity at the desired frequency) to the 780-nm light using a fiber EOM from EO Space. The cavity reflection is used as input to our cavity lock. We use a Superlaserland digital servo, designed by the National Institute of Standards and Technology (NIST) [39], to feedback to the cavity piezo (see Fig. 8).

Next, the stabilized cavity is used to lock the “parent” 370-nm laser (Toptica DL PRO), also using a PDH lock. 19.76-MHz sidebands are added to the light using a free-space Qubig EOM. The cavity reflection is mixed with a stable frequency source equal to the applied sideband frequency, and the resulting signal is used to lock the laser via a Toptica DLC-PRO Lock. The frequency of the parent laser is chosen to be roughly centered between the  $^{171}\text{Yb}^+$  and  $^{174}\text{Yb}^+$  Doppler cooling transitions. Therefore, the same locking electronics can be used to lock 370-nm experiment

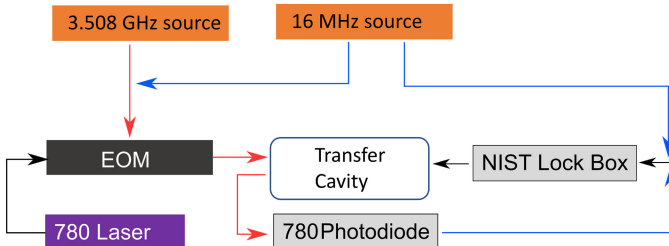
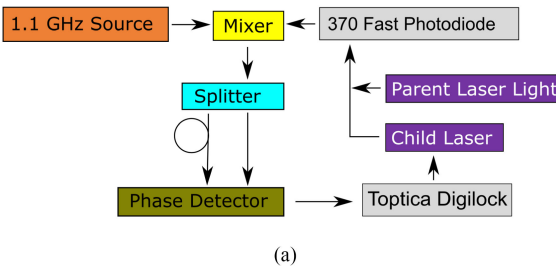
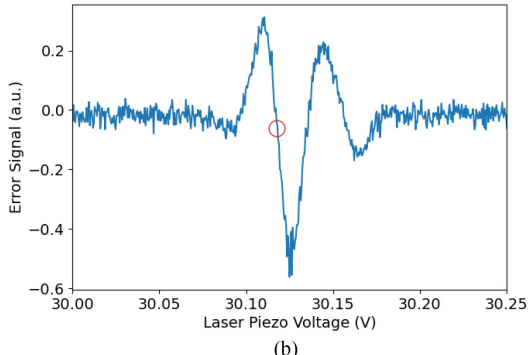


**FIGURE 8.** Electronic components used to lock the transfer cavity to the stabilized 780-nm laser. It is a Pound-Drever-Hall lock [37], [38], where 16-MHz sidebands are added and then demodulated from a signal to yield a sharp locking feature.



(a)



(b)

**FIGURE 9.** Locking electronics and signal for 370-nm child laser beatnote lock. (a) Beatnote lock schematic for stabilizing child laser frequency relative to parent laser (amplifiers and filters not shown). (b) Signal used for locking the child 370-nm laser generated from the electronics in (a). We lock to the downslope of the dip with the highest contrast, as marked with the red circle.

lasers to either isotope for diagnostics, calibration, or perhaps sympathetic cooling [40], [41]. Light from the parent 370-nm laser is split in free space and then coupled into fibers that are sent to various experiments and a Toptica High Finesse wavemeter (HF-ANGS WS8-2+1X8PCS) for monitoring.

## 2) LASER BREAKOUT BOARD WITH BEATNOTE LOCK MODULE

The final laser is the “child” 370-nm laser (Toptica DL-PRO), which is shown on the breakout board in Fig. 10. A small portion of the light from this laser ( $\sim 50 \mu\text{W}$ ) is split off and sent to a 50/50 beamsplitter, where it is combined with light from the parent 370-nm laser. The combined light is coupled into a fiber and sent to an AlphaLas Si Photodetector (UPD-50-UP-FR-F). The beatnote from the light is mixed

with a stable 1.125-GHz reference frequency provided by a Vauxix lab brick and filtered to produce a beatnote signal [42]. The Toptica DLC-PRO Lock electronics perform a side-of-fringe lock on the beatnote signal to set the frequency [see Fig. 9(b)].

The breakout board also sends the light through an IntraAction AOM, which serves as a switch to add extra extinction to the 370-nm light on the ion as needed. The first-order output from the AOM is coupled into a fiber and sent to a modulation board. The zeroth-order output is sent to the wavemeter for monitoring.

## 3) MODULATION BOARD

At the modulation board, the 14.7- and 2.105-GHz signals are added to the 370-nm light, as outlined in Table 1. As shown in Fig. 10, the light is first directed to the free-space QubiQ EOMs [43] after which it is split into two paths. Each path goes through a double-passed AOM for wideband (up to  $\approx 50 \text{ MHz}$ ) frequency control and then coupled into a fiber that is sent to the experiment. There are two 370-nm beam paths available for diagnostics and loading assistance, but ultimately only one path is used for cooling, pumping, and detecting the ions.

## 4) LIGHT DELIVERY

Once at the experiment, light exits the fiber and focuses on the ion. Our current layout has two 370-nm beams each at a  $45^\circ$  angle with the axis of the trap. The  $\vec{k}$ -vector of these beams and the principal axis rotation of the ions in the trap were chosen, so each path is able to cool all three secular frequency directions (see Fig. 11). The 399-nm light also makes a  $45^\circ$  angle with the trap axis, while the 935-nm light and the 760-nm light are directed along the axis of the trap. The magnetic field is parallel to the  $\vec{k}$ -vectors of the 355-nm beams and is supplied by permanent magnets (see Section VII-A).

We chose lenses to yield a specific spot size at the ion, such that some beams are elliptical while others are round based on their purpose and angle of incidence. Table 2 summarizes the lenses chosen for each beam and the expected beam size at the ion. For the elliptical beams, the shorter focal length cylindrical lens determines the size of the beam in the direction perpendicular to the trap. The longer lens is aligned so the ion is several millimeters behind the focus of the beam and controls the beam size parallel to the trap. This arrangement results in a beam with minimal scatter on the trap surface, but large enough extent to simultaneously address multiple ions.

We also created custom pieces to stably hold our beam launch optics, which can be seen in Fig. 12. The mounts each start with a Newport 561D-XYZ ULTRALign stage attached to a custom adapter plate that has a hole pattern allowing us to match the stage position to the holes of the optical breadboard (which differs depending on the position around the chamber). Next, a custom L-bracket is attached to the

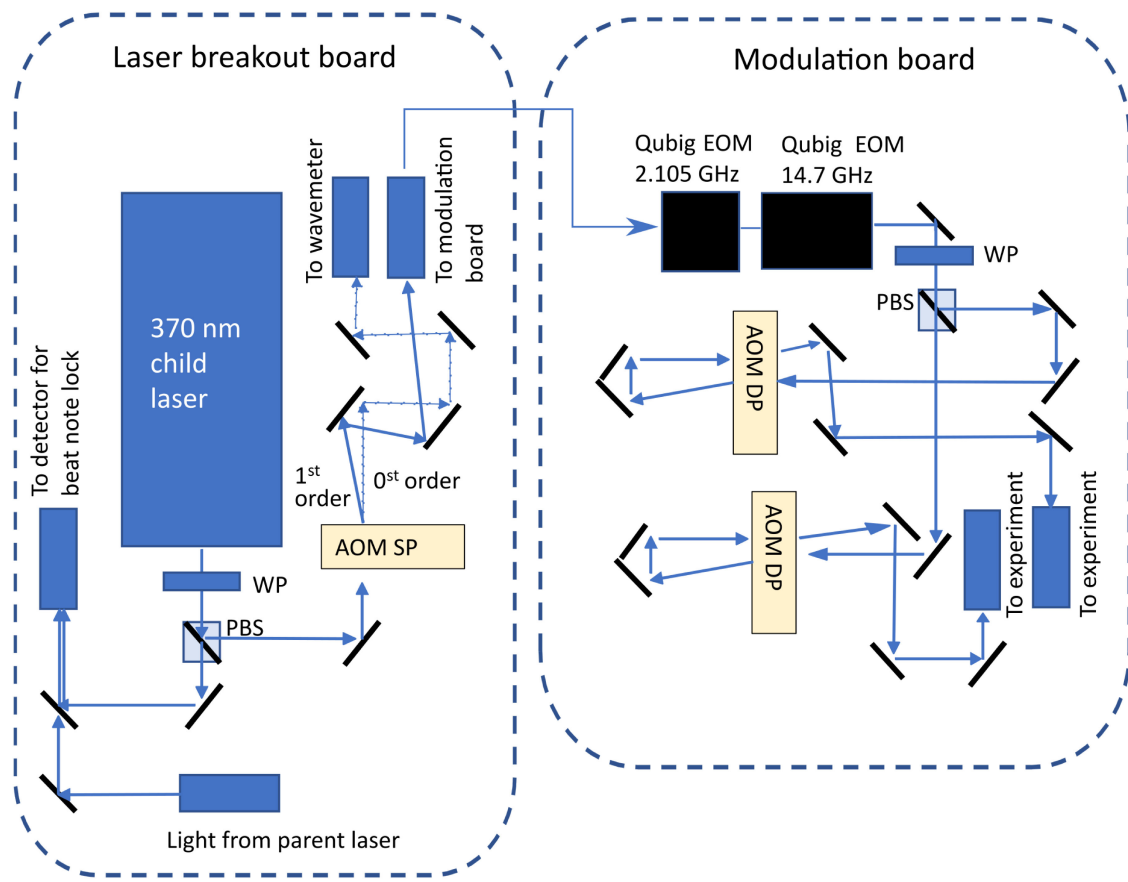


**FIGURE 10.** Schematic of 370-nm breakout board (left) and modulation board (right). PBS indicates a polarizing beam splitter, WP is waveplate. AOM SP indicates an acoustooptic modulator in the single pass configuration, while AOM DP is in the double pass configuration (also apparent from the beam path arrows).

**TABLE 2.** Optical Components Used for cw Light Delivery to the Ion

Beam (nm)	Collimator	Shape	Focusing lens (mm)	Lens-ion distance (mm)	Waist at ion ( $\mu\text{m}$ )
370	$\mu$ laser FC10	Round	150	150	6
370	$\mu$ laser FC10	Elliptical $\perp$ trap Elliptical $\parallel$ trap	cyl 150 cyl 200	150 240	6 140
399	$\mu$ laser FC5	Round	250	250	32
435	$\mu$ laser FC10	Elliptical $\perp$ trap Elliptical $\parallel$ trap	cyl 150 cyl 200	150 242	7 150
935 and 760	ThorLabs RC02FC-P01	Round	250	250	74

Waist is the  $1/e^2$  intensity radius and “cyl” indicates a cylindrical lens.

vertical short side of the translation stage, which holds a goniometer for adjusting the beam’s angle (“tip”) as it is focused on the trap. On top of the goniometer is another custom piece, which serves as the adaptor to a Thorlabs cage mount system. For the cage mount rods, we use carbon fiber instead of steel for its stiffness and low temperature sensitivity (though it is unclear if this has been beneficial). The cage system holds and centers the collimators with the

lenses and waveplates necessary for light delivery. We use Newport picomotors for remote position adjustment in  $x$  and  $y$ .

#### IV. LASER-BASED QUBIT STATE MANIPULATION

While incoherent techniques for manipulating ions, as outlined in the previous section, are important for cooling,

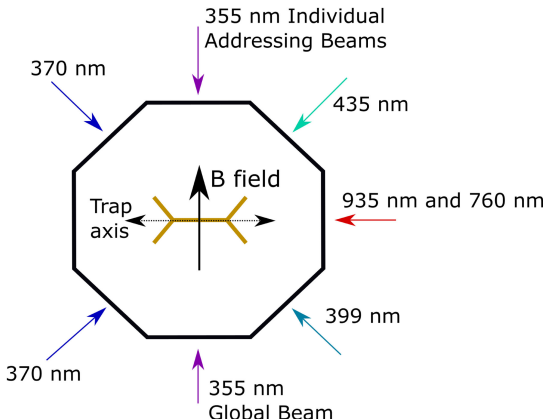


**FIGURE 11.** Schematic of chamber as seen from above, showing layout of lasers. The gold “bowtie” in the center of the chamber shows the trap orientation and the arrow labeled “B field” shows the direction of the magnetic field.

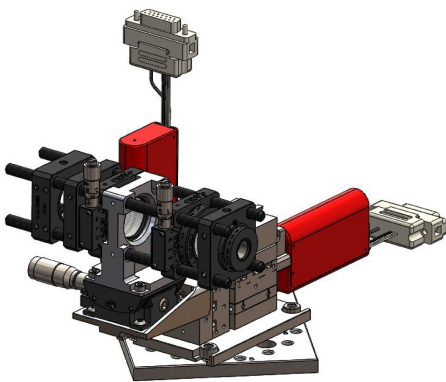


**FIGURE 12.** Example fiber launch assembly, showing custom pieces for attaching the translation stage to the breadboard, attaching the goniometer to the side of the translation stage, and attaching the cage assembly above the goniometer.

state preparation, and detection, quantum computing requires *coherent* manipulation of qubit states. As mentioned previously, we use the  $^{171}\text{Yb}^+$  hyperfine clock transition ( ${}^2\text{S}_{1/2}|F=0,m_F=0\rangle \rightarrow |F=1,m_F=0\rangle$ ) as the qubit states, depicted in Figs. 4 and 13). The frequency between the two qubit states is given by  $f_{\text{qubit}} = 12.642812118466 \text{ GHz} + \delta_{2z}$ , where  $\delta_{2z} = (310.8)\text{B}^2 \text{ Hz}$ , where  $B$  is the magnetic field in Gauss [7]. The frequency to first order is insensitive to magnetic fields when  $B$  is small. This magnetic field insensitivity and the fact that T1-type decay between states in the  $S$  manifold is extremely rare contribute to extremely long coherence times [8], which are necessary for high-fidelity operations and large circuit depths. While these states can be directly manipulated with microwaves, individual addressing and two-ion interactions with microwaves require sophisticated techniques to create localized microwave fields and gradients [44], [45]. Instead, we use a laser to perform single-ion and two-ion gates, so we can take advantage of tight focusing and specific beam

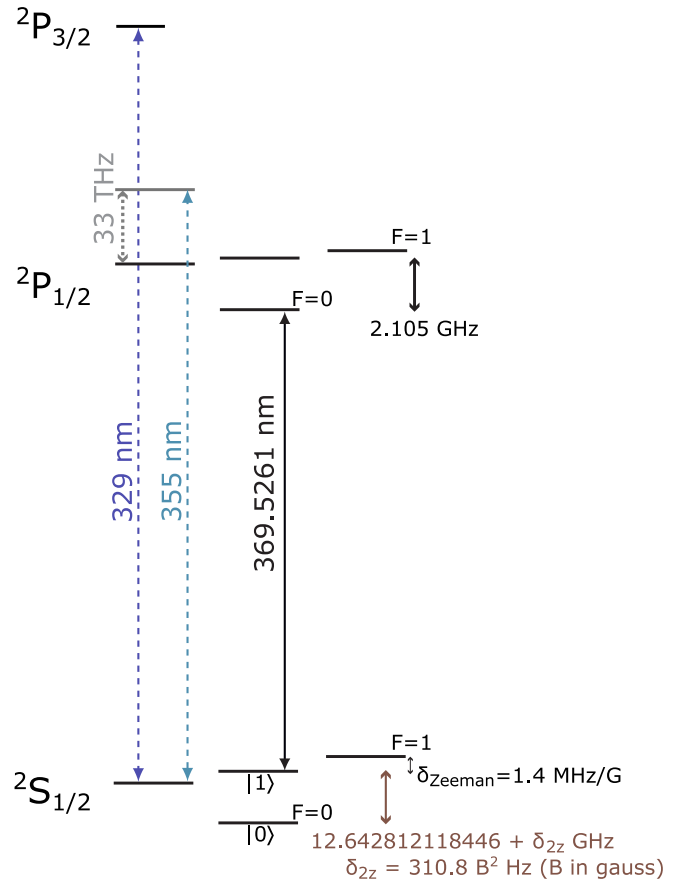


**FIGURE 13.** Cartoon of the relevant energy levels for the Raman transition in  $^{171}\text{Yb}^+$ . The 355-nm light used in the Raman beams spans from the  ${}^2\text{S}_{1/2}$  state to a virtual state (gray) between the two  $P$  levels, approximately 33 THz from the  ${}^2\text{P}_{1/2}$  state. By careful selection of the comb teeth used in the pulse laser, we span the 12.643-GHz offset between the  $|0\rangle$  and  $|1\rangle$  states of the qubit without high-frequency electrooptical components or a second laser.

geometries to create the field gradients necessary for individual addressing and two-qubit gates mediated by a phonon bus [46]. Specifically, we use a 355-nm pulsed laser that drives two-photon Raman transitions [47], [48] via a virtual state, 33-THz detuned from the  ${}^2\text{P}_{1/2}$  level (see Fig. 13). We chose to use a pulsed laser because the frequency comb associated with a train of pulses has sufficient bandwidth to span the qubit transition frequency [15].

#### A. PULSED 355-NM LASER

We use the Coherent Paladin Compact 355 as our pulsed Raman laser. It is a commercial laser that has a repetition rate around 120 MHz [49] with individual pulses roughly 15 ps long. The pulse repetition rate was selected such that no pair of frequency comb teeth generated by a single pulse train would be resonant with any transition in  $^{171}\text{Yb}^+$ . This includes the carrier transitions ( ${}^2\text{S}_{1/2}|F=0,m_F=0\rangle \rightarrow |F=1,m_F=0\rangle$ ), the estimated radial and axial sidebands, the Zeeman hyperfine transitions ( ${}^2\text{S}_{1/2}|F=0;m_F=0\rangle$  to  ${}^2\text{S}_{1/2}|F=1;m_F=-1\rangle$  or  ${}^2\text{S}_{1/2}|F=0;m_F=1\rangle$ ) and

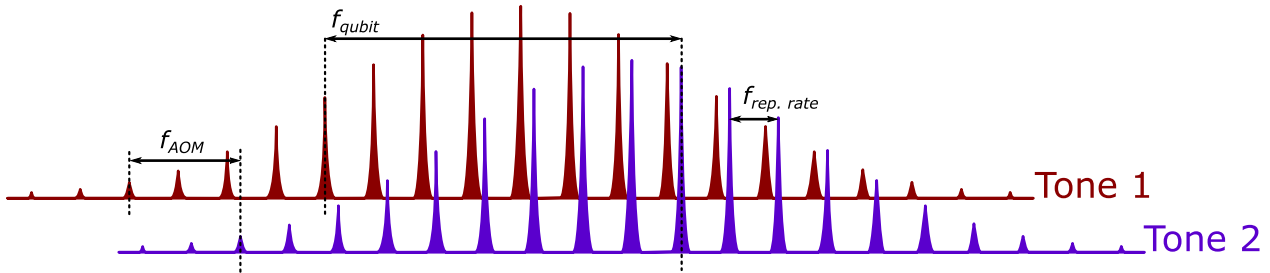


**FIGURE 14.** Graphical representation of the AOM-shifted frequency comb and repetition rate feedforward scheme. To drive ion transitions, two frequency combs offset by  $f_{AOM}$  are applied to the ion, such that different teeth in those combs span the frequency separation of the desired transition, labeled  $f_{qubit}$ .

the so-called micromotion sidebands, which consist of any transition  $\pm$  the trap rf drive frequency (usually 35–85 MHz for  $^{171}\text{Yb}^+$ ). Additionally, the Paladin laser has an average output power of 3.75 W, which is sufficient to split the beam multiple times (see Section IV-C2) and still have enough power to drive Raman carrier transitions on each ion at a 500-kHz Rabi frequency. The output power of the laser is internally stabilized against slow drift; thus, we only need to stabilize the beam intensity on fast times scales, which is accomplished by feeding back on a small portion of the beam. However, the pulse repetition rate, which is critical for defining the frequency combs used to perform transitions, is not internally stabilized and is expected to drift a few kilohertz over the course of the day. This can be corrected for by implementing a feedforward system, as described in the next section and in Section VI-A2.

### B. LOCKING

To drive transitions between the  $|0\rangle$  and  $|1\rangle$  states of the qubit, we need two frequency tones that are separated by 12.643 GHz, the resonant frequency of the transition. Because we have carefully selected our laser repetition rate to precisely *not* overlap with any transitions, we spatially overlap at least *two* offset frequency combs in order to create the necessary frequency separation to drive transitions (see Fig. 14). For example, assuming a repetition rate,  $f_{rep}$ , of exactly 120 MHz, the first and 105th comb lines nearly span the transition frequency. However, there is a 42.8-MHz offset,  $f_0$ , from the qubit transition to the comb separation. To bridge this gap and drive the carrier transition, we apply a relative frequency shift,  $f_0 = f_{qubit} - n \times f_{rep}$ , between the two frequency combs using AOMs, where  $n$  is a fixed ratio (see Fig. 14). Depending on the desired transition, the applied frequency offset of the combs may vary.

Because the laser cavity length sets the repetition rate and thus the frequency comb spacing, it is sensitive to thermal drift, such that  $f_{rep} \rightarrow f_{rep} + \delta f_{rep}$ . In order to maintain a fixed frequency offset between the two tones, we actively track the variations in repetition rate and add an additional correction,  $n \times \delta f_{rep}$ , to the frequency offset that is applied to the AOM [15]. To achieve maximum sensitivity to frequency

drift, instead of simply measuring the repetition rate, we measure a higher order harmonic  $\tilde{f}_{rep}$ . Specifically, we measure the 32nd harmonic because it is the highest harmonic we can reliably detect within the measurement range of our photodiode (Hamamatsu S9055-01). The signal from the photodiode goes through a custom bandpass filter to select the 32nd harmonic and is mixed with a stable frequency reference (Wenzel 3.7 GHz MXO-PLD). The resulting mixed frequency is tracked by our rf control hardware (see Section VI-A2). Any deviations from the expected repetition rate are scaled by  $n$  (such that  $n\delta f_{rep} = n\delta \tilde{f}_{rep}/32$ ) and added to (or subtracted from) one of the multiple rf tones applied to the AOM.

### C. OPTICAL BEAM PATHS

As discussed in the previous sections, our qubit operations are performed using two-photon Raman transitions. Since there are two photons involved, the beam propagation direction(s),  $\vec{k}$ , determines how much total momentum is imparted on the ion, which can cause the ion to interact with particular motional modes of the ion trap. For example, copropagating beams are only weakly sensitive to the ion motion or temperature because  $\Delta k \approx 0$ . Any other configuration yields  $\Delta k \neq 0$  and results in a momentum kick imparted to the ion, which is necessary for sideband cooling and driving Mølmer–Sørensen (MS) gates [46]. We have chosen to use counterpropagating beams along the surface of the device, perpendicular to the ion chain axis, for driving gates that require a momentum kick. In the counterpropagating configuration, momentum transfer is maximized ( $\approx 2|\vec{k}|$ ) and since we are perpendicular to the trap axis, momentum transfer is only possible to the radial modes of the ion (and to first order, gives no access to the axial modes).

The counterpropagating configuration requires two optical beam paths be directed to our ion chain. When designing these optical beam paths, there are several considerations.

- 1) Individual pulses from the laser are 15 ps long; thus, for the pulses to overlap at the ion from separate beam paths, the beam path lengths must match on the sub-millimeter scale.
- 2) Relative beam path lengths must not change due to vibrations or air currents.

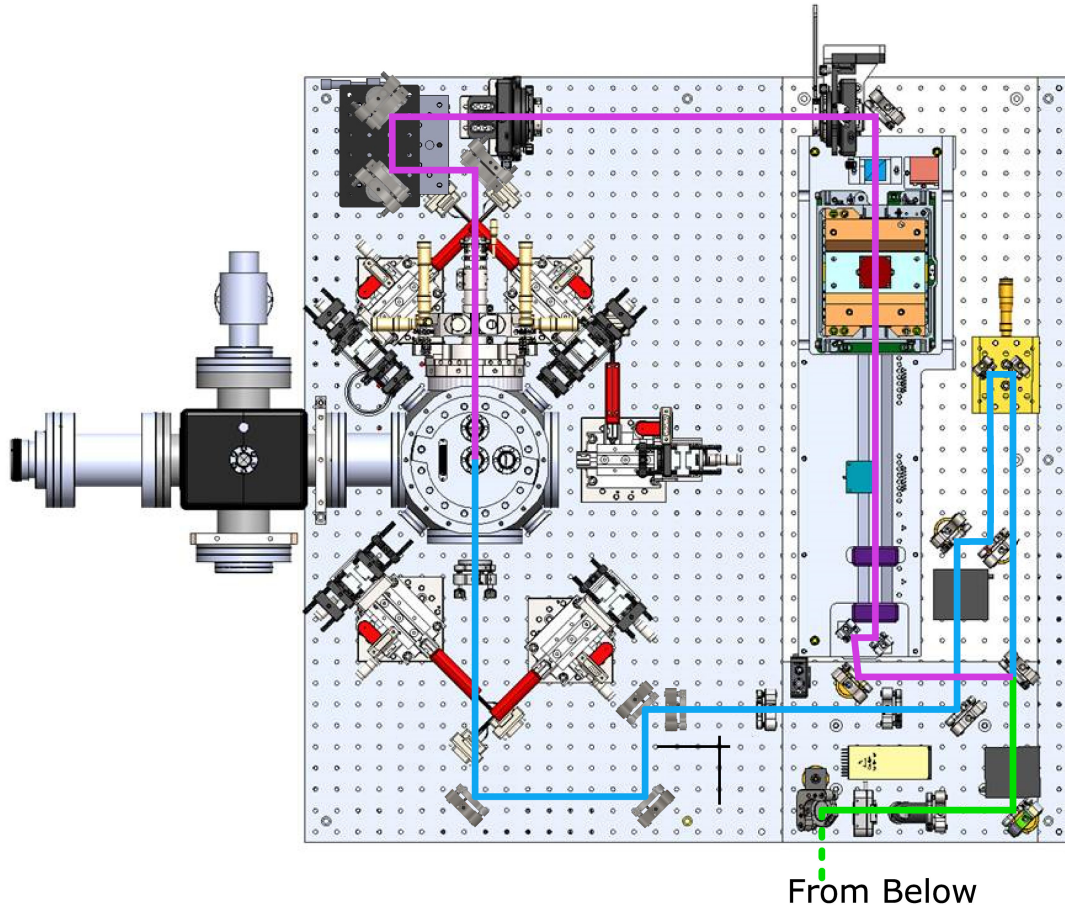


**FIGURE 15.** 3-D rendering of the optical path for the Raman beams as seen from above. The chamber is mounted to an optical breadboard, with the laser on the optical table below it (not shown). The shared path between the global and individual setups is shown in green, where the light travels from the laser below through the optical breadboard and then passes through polarization optics to set the total laser power and to an AOM, which is used for power stabilization. Then, the light passes through a beamsplitter, where it is split into the two separate paths. The global path (teal) goes to a mirror pair mounted on a stage allowing for path length matching of the beams and then its own AOM for frequency control. The individual addressing beam path (magenta) passes through the 32-channel Harris AOM, where it is first split into 33 beams by a diffractive element. Each beam goes to its own AOM crystal, which modifies the frequency, amplitude, and phase of that beam based on the driving rf signal. After the AOM in each path, there are optics to shape the beams and image all frequencies to the same locations at the ion chain. Also shown are the placement of cw-laser beam delivery subsystems around the vacuum chamber.

- 3) We must be able to shift the frequency combs relative to each other in frequency space to address different transitions.
- 4) Copropagating and MS gates require two frequency combs from the same direction; thus, alignment needs to hold for a broad range of frequencies.
- 5) At least one of the beam paths must be able to individually address the ions.
  - a) Each ion requires a laser with distinct frequency, amplitude, and phase control.
  - b) Beams must be tightly focused to not overlap with nearby ions.

In the following, we will describe our design and how it allows us to achieve the above requirements. A schematic of the beam paths is shown in Fig. 15. The beam paths include a method for: path length matching on the micrometer

scale; carefully designed optical mounts to prevent vibrations; AOMs in both paths to shift the frequencies; optics designed to reimaging a wide range of frequencies; one path with multiple beams with independent control of frequency, amplitude, and phase; and finally, optics to create tightly focused beams at the ions with low crosstalk and scatter. To minimize air currents and other environmental disturbances, the entire system is enclosed.

### 1) GLOBAL BEAM DESIGN

The global beam (represented by the teal beam in Fig. 15) is designed to work either alone, to drive motionally insensitive gates on the entire ion chain, or, with individual beams, to drive motionally sensitive gates on specific ions. To that end, the beam needs to have a nearly uniform spatial profile, the alignment must be stable, and the timing must be aligned to the individual beams.

After splitting the individual path and the global bath at a beam splitter, the global beam is diverted to a pair of mirrors on a linear translation stage to allow for fine-tuning of the path length without affecting downstream beam alignment. Next, the beam passes through an AOM, allowing for full amplitude, phase, and frequency control of the beam.

To select the global beam size, we needed to ensure that we would not scatter on the surface of the trap and that we would be able to roughly equally illuminate 32 ions. We calculated that a Gaussian horizontal beam with a waist of 160  $\mu\text{m}$  spans 32 ions with a 4.5- $\mu\text{m}$  ion spacing with less than 1% power variation over the center three ions. Vertically, since the ion is about 70  $\mu\text{m}$  away from the trap surface, a round beam with a waist of 160  $\mu\text{m}$  would scatter on the surface, likely resulting in trap charging, stray reflections, and degradation of beam quality at the ion. Thus, the global beam was chosen to have an elliptical shape. Since the isthmus of the trap is 1.2 mm and the beam has a Gaussian profile, for the global beam to have maximum clearance from all trap surfaces and remain centered on the ion, the vertical beam waist should be 8  $\mu\text{m}$  at the ion. Thus, we chose an elliptical beam with 8  $\mu\text{m} \times$  160  $\mu\text{m}$  at the ion to minimize scatter but still equally illuminate the ions.

To achieve these beam waists, we use a cylindrical telescope to change the aspect ratio of the beam by using a concave/convex lens pair, which avoids putting the beam through any unnecessary focal planes. A spherical lens is used to reimagine the beam near the final focusing optics to minimize the effects of vibrations and diffraction.

## 2) INDIVIDUAL ADDRESSING BEAM PATH

The individual addressing beam path is more complicated than the global beam path, due to the extra requirements of splitting the beam many times, separately controlling each beam, and then imaging each beam on one and only one ion.

We use an illumination module from Harris Corporation, which is a multichannel AOM, which was specifically designed for this application [50] and pioneered at the University of Maryland [51]. It has integrated diffractive optics that splits the single beam into 33 equal and parallel beams, which are sent to 32 separate integrated miniature AOMs (the last beam is blocked internally). Each AOM has an independent rf input from a dedicated rf amplifier. The control signal to the amplifier is generated by an rf system on chip (RFSOC) (or an Octet; more details are in Section VI). It can generate multitone rf signals with arbitrary amplitude, frequency, and phase modulation capabilities, which allows us to exercise complete control over the light applied to each ion. However, the AOM also deflects the beam depending on the applied rf frequency (in our case, vertically). To prevent these deflections from causing different frequencies to have different overlap with an ion, light from the AOM needs to be carefully reimaged onto the ion.

The output of the multichannel AOM consists of 32 parallel beams with an 80- $\mu\text{m}$  waist and a 450- $\mu\text{m}$  pitch. To image these onto the ions, the pitch of the AOM needs to be

matched to the 4.5- $\mu\text{m}$  pitch of the ions resulting in a 0.8- $\mu\text{m}$  beam waist. However, as discussed previously in the global beam design, due to the trap geometry, an 8- $\mu\text{m}$  beam in the vertical direction is ideal for minimizing scatter from the surface of the trap. Thus, we require an oval beam at each ion with a 0.8- $\mu\text{m}$  axial (horizontal) waist and an 8- $\mu\text{m}$  vertical waist. The reimaging and beam shaping are accomplished using a combination of off-the shelf and custom optics, some of which are prealigned and bonded in place to make alignment of the entire beam path easier, as described in the next paragraph. Additionally, the optical path was designed to keep the beams compact to minimize the effect of air currents causing variations between the beams or along a single beam.

After the AOM, the beams immediately go through a pair of cylindrical lenses, designed to change the aspect ratio of the beam to the desired 10:1. These lenses were centered using an air-bearing/autocollimator alignment station [52], [53] to ensure that their optical axes were exactly aligned before being bonded into custom mounts. The cylindrical lens assembly was mounted to the breadboard using a Newport LP-1A for  $x$ ,  $y$ , tip, tilt, and roll position control. The cylindrical pair is followed by a spherical lens, bringing the beams to a focus, that is reimaged by a spherical pair combined with a custom lens assembly from PhotonGear (PN:PG-18020-S) [10], [54]. The PhotonGear lens relay has a 44.4-mm housing-to-image distance and a numerical aperture (NA) of 0.16 on the ion side and 0.04 on the input side. It has also been designed to account for the 3-mm-thick vacuum window, additionally compensating for the aberrations caused by the window bowing while it is under vacuum. To minimize aberrations at the ion, it is extremely important that the lens is aligned normal to the window surface, which is not necessarily parallel to the ion chain. This alignment is particularly difficult because the relay lens is entirely inside the re-entrant bore window when it is the correct distance from the ion. Additionally, the alignment of the spherical pair and the lens relay is crucial for setting the magnification. Therefore, to hold and align these lenses relative to each other and to the ion, we designed and built a custom five-axis flexure mount.

The flexure stage is shown in Fig. 16. It is bolted directly onto a mounting ring on the re-entrant window, registering the lenses to the center of the chamber. Hidden from view in the photo is the relay lens itself, because it is entirely inside the re-entrant bore. The flexure design uses opposing micrometers to align the position in  $x$  and  $y$ , which can then be brought together to lock the mount in place. The range of motion is designed to cover the full length of the trap, if necessary, but, currently, the individual addressing beams are aligned to the trap center. Tip and tilt are controlled by the three additional micrometers accessible on the front of the mount and allow us to reduce aberrations by matching the tip and tilt of the lens to the tip and tilt of the vacuum window. A pair of spherical lenses are centered with respect to the relay lens with the air-bearing/autocollimator alignment station, as

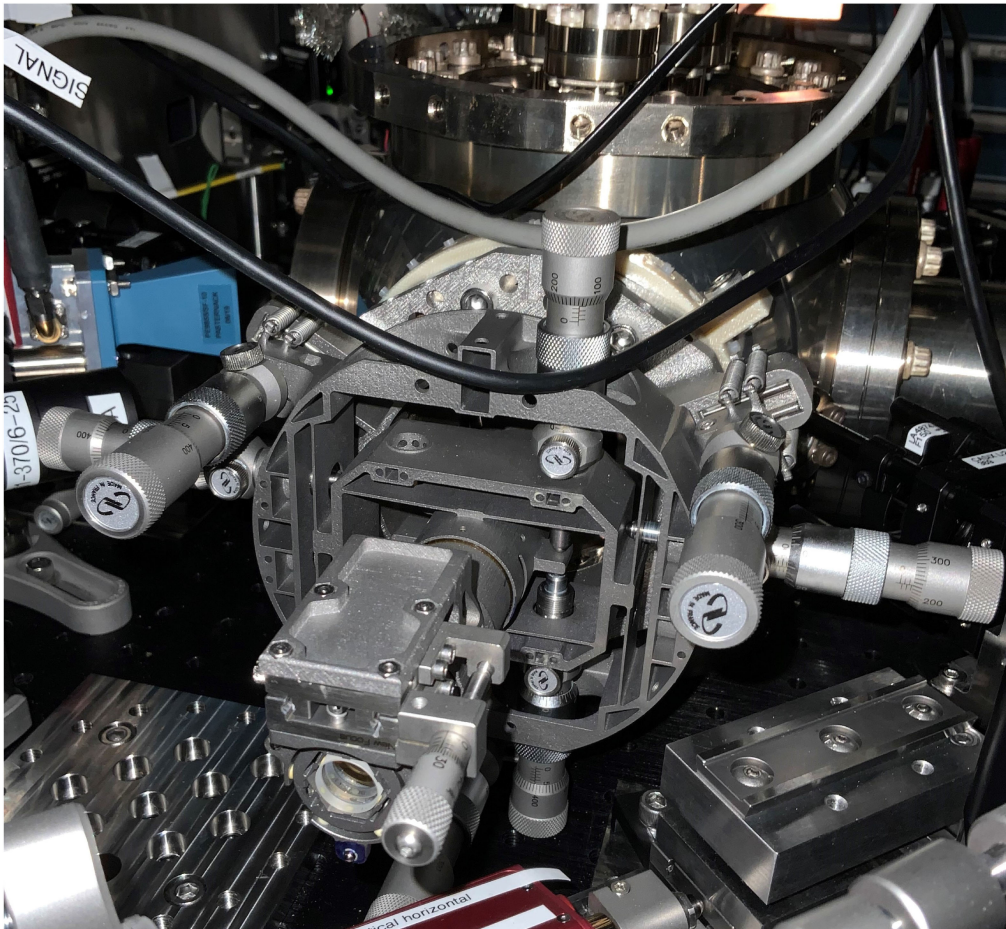


**FIGURE 16.** Image of the five-axis flexure mounted onto the individual addressing re-entrant flange. The parts are 3-D printed from titanium and steel and then assembled before adding the lenses. The optics are aligned to the optical center of the lens (rather than the mechanical center) using external hardware and then bonded in place. By completing relative alignment of the optics, before mounting the flexure stage, we realize greater optical precision than we could achieve by hand. This lends to the achievement of the desired beam waist with few aberrations.

mentioned previously. They are bonded to a translation stage, which allows for small adjustments to the focal position, but they are mechanically linked to, and optically centered on, the lens relay. By actively aligning the lenses to the lens relay on the same mount, we have created a single larger objective simplifying the alignment procedure.

#### D. BEAM CHARACTERIZATION

To determine the quality of our optical alignment, we characterize the beam profile at the ions. For the global beam, a beam profiling camera at the ion location can be used (before the chamber is sealed and baked for vacuum). We measured a beam waist of  $10.9 \mu\text{m}$  vertically and  $182.8 \mu\text{m}$  horizontally, which is close to the desired  $8 \mu\text{m}$  by  $160 \mu\text{m}$  beam size. However, the individual beams are much smaller than the pixel size of our beam profiling camera, so we must use the experiment itself to characterize those beams. First, by taking advantage of the high-resolution imaging system, we can align the beams to the trap surface and check each one for general shape and size (see Fig. 17). After aligning to the

trap surface, it is straightforward to align to an ion by lifting the beams away from the trap surface using a micrometer.

We can shuttle the ion through the beams and extract horizontal beam profiles by driving qubit rotations and averaging the number of detection counts per ion position (200 repetitions per point). The ion position is controlled by voltage solutions that are precisely calculated to a submicrometer scale, resulting in a more accurate measurement of the beam profiles along an ion chain, shown in Fig. 18. The beam profiles confirm that the beam waists and spacings are roughly consistent with the design and that there are no obvious aberrations.

##### 1) CROSSTALK

Linear chains of ions spaced closely together have stronger Coulomb interactions, which lead to larger frequency spacings of the motional modes and is advantageous for the practical implementation of fast two-qubit gates. However, having neighboring sites close together increases the probability of optical crosstalk. We measure the impact of the

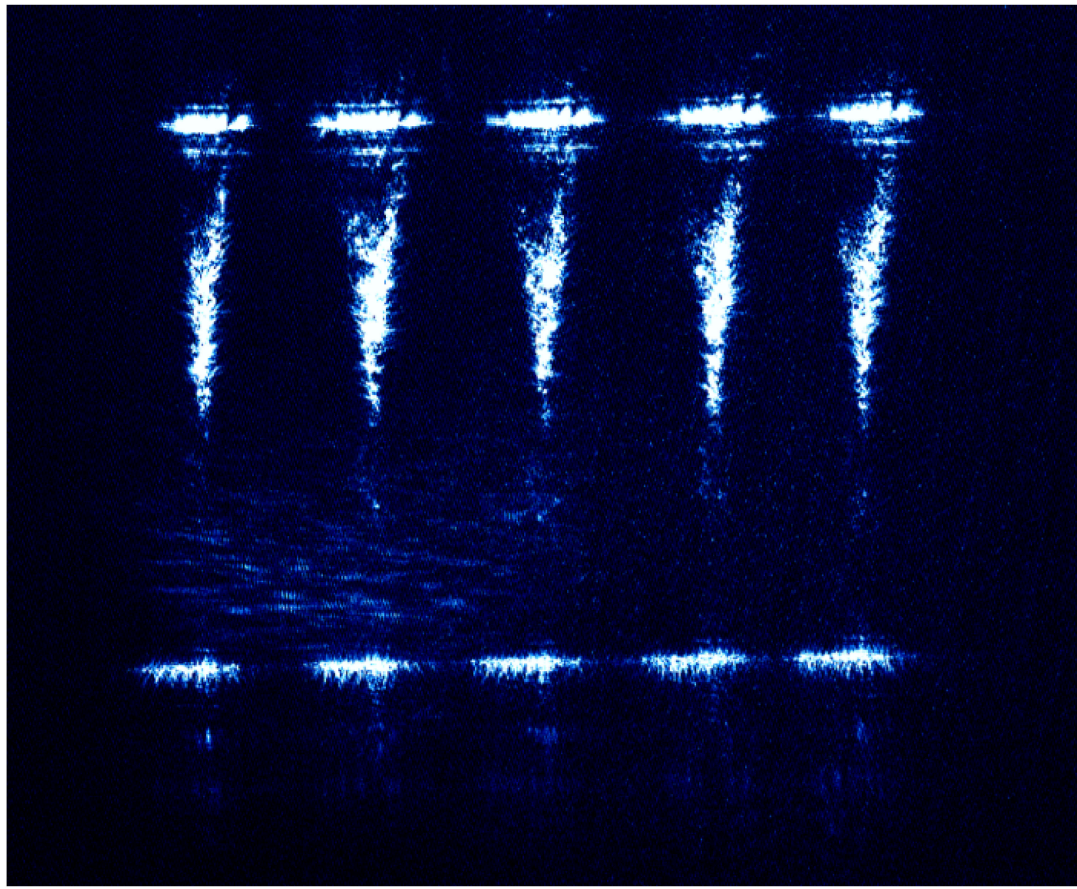


**FIGURE 17.** Image of the individual addressing beams skimming across the trap surface. The horizontal features are where the reflected scatter is increased at the edge of trap electrodes. The bottom lines are at the edge of the slot on an HOA trap and the top is the edge of the rf rail. The vertical cones are the beams reflecting from the surface of the trap slightly after the beam waist. This shows beams 1, 8, 16, 24, and 32 (out of 32) from left to right. The imaging system is not designed to be fully diffraction limited at 355 nm and is limiting the resolution of this image, causing the beams to appear fuzzy and jagged, which is not a faithful representation of the beam profiles.

neighboring beams at our  $4.5\text{-}\mu\text{m}$  spacing by taking advantage of our ability to shuttle the ion. First, we drive Rabi oscillations using three consecutive individual addressing beams and measure the Rabi frequency at each beam position to ensure they are close to equal. Then, turning on only the center beam (centered at  $0\text{ }\mu\text{m}$  in Figs. 18 and 19), we measure the Rabi frequency as a function of ion location. Fig. 19 shows the scaled Rabi frequency as a function of ion location, where the measured frequencies are normalized to the maximum observed Rabi rate at position  $0\text{ }\mu\text{m}$ . The decay of optical crosstalk from the center location is empirically fit to a Lorentzian distribution. We do not see any enhancement of the crosstalk above our baseline at the locations of the neighboring beams, suggesting minimal amounts of electrical crosstalk or acoustical crosstalk from the AOM. We measure optical crosstalk of the neighboring site at about  $2.3(6)\%$  and at the next nearest neighbor site =  $0.6(2)\%$ . To reduce the effects of the crosstalk, a cancellation tone can be applied to the neighboring channels (see Section VI-A5).

## V. ION IMAGING AND DETECTION

Another piece of hardware for our quantum system is the measurement and detection scheme. As described in Section III, detection is performed by illuminating ions on resonance with a cycling transition accessible to only one of the qubit states. The resulting ion fluorescence is collected, and depending on the number of photons captured in a particular time, we determine whether the ion is in the  $|0\rangle$  (dark) or  $|1\rangle$  (bright) state (see Fig. 4). The bright and dark state histograms for repeated measurements ideally do not overlap, and we can distinguish the states with a high degree of accuracy [55]. Due to our imaging systems' photon collection efficiency of  $\approx 0.5\%$  (number of photons collected by the detectors/number of photons produced by the ion), our detection time is set to  $350\text{ }\mu\text{s}$ . During this time, we collect about 12 photons from an ion in the bright state and 0 or 1 photons from an ion in the dark state (on average 0.004 photons from an ion in the dark state). Naively modeling the bright and dark states as Poissonian distributions centered at 12 and 0.004, respectively, we calculate an error  $<8\text{e-}5$  of bright ions appearing dark and an error  $<8\text{e-}6$  of dark

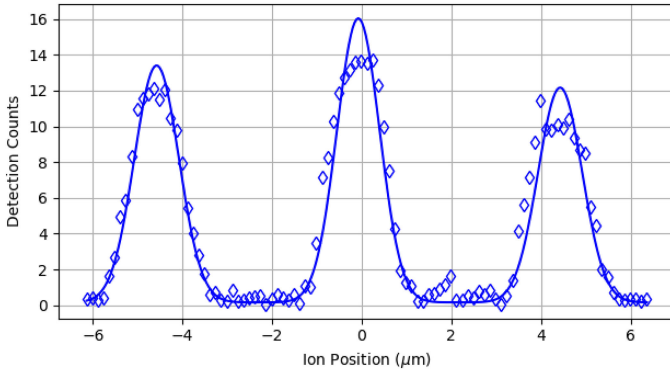


**FIGURE 18.** Average number of counts seen on a detector during a 350- $\mu$ s detection cycle as the ion is moved through the individual addressing Raman beams of a fixed pulse duration and power. Fitting the raw counts to generic Gaussian peaks, we estimate the beam waist is roughly 0.8  $\mu$ m with no obvious aberrations. We also confirm that the spacing between the beams is 4.5  $\mu$ m consistent with the 0.8- $\mu$ m beam waist.

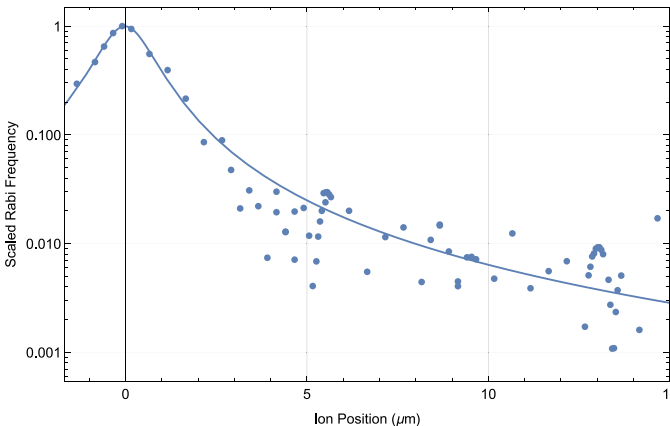


**FIGURE 19.** Optical crosstalk is determined by the relative Rabi frequency measured when an individual addressing beam is interrogating a neighboring site. By measuring the Rabi frequency versus ion position using counterpropagating Raman beams, we determine the optical crosstalk value to be 2.3(6)% at the neighboring beam location and 0.6(2)% at the next nearest neighbor site. We do not see any clear evidence of electric or acoustic crosstalk on neighboring AOM channels causing an increase in the crosstalk at the ion. The solid line is an empirical Lorentzian fit with a full-width half-max of 1.29  $\mu$ m.

ions appearing bright due to overlap of the distributions. In addition to the distribution overlap, there are errors due to off-resonant coupling induced by the detection beam. During a detect time of 350  $\mu$ s, an ion in the bright state has a 1.7e-2 probability of off-resonant coupling to the incorrect  $P$  state followed by decay to a dark state (similarly there is a 1e-3 probability of a dark ion off-resonantly coupling to the bright state). Depending on the number of photons collected before off-resonant coupling events, they do not necessarily result in detection errors.

The thresholding technique is very good for a single ion. However, when there are multiple ions, the histograms generated from repeated measurements of two bright ions and one bright ion overlap considerably. At larger numbers of

ions, distinguishing between the numbers of bright ions becomes even more challenging. Additionally, for quantum algorithms, it is important to know *which* ions are bright and dark, instead of just the pure number of bright ions.

To address these issues, each ion has a dedicated PMT to determine if that particular ion is bright or dark. Dedicated PMTs provide increased sensitivity and readout speed compared to commonly available cameras and less crosstalk between channels as compared to a PMT array. To get light to individual PMTs, we image the ion light into a multicore multimode fiber (see Fig. 20). This fiber has 32 separate 50- $\mu$ m-diameter cores spaced 125  $\mu$ m apart (FiberTech Optica, custom), with light from each ion aligned to a distinct core. The cores are then broken out into individual fibers [see Fig. 20(a)], and each fiber plugs directly into a separate PMT (Hamamatsu H10682-210, dark count average 20 per second).

For additional diagnostics, we have a camera (Andor Luca DL-604M-#VP) and a free-space coupled global PMT (see Fig. 21). The camera has an approximately 250- $\mu$ m total field of view along the axis of the trap and is typically used for alignment. The global PMT also has a large field of view and works well for single ion diagnostics and rough alignment. These are each accessible via remote controlled motorized flip mirrors (also shown in Fig. 21).

Since the fiber cores are spaced by 125  $\mu$ m and the ions are spaced by 4.5  $\mu$ m, we need to reimaging the light from the ions onto the cores. To do so, we use a two-stage imaging system. The first stage is a PhotonGear imager (PG-15470-S\_A) with an NA of 0.6 to collect light from the ions. There is a re-entrant window in the vacuum chamber (described in Section II) in order to place the imager at the proper distance from the ion (11 mm total, including a 4-mm fused silica window). We adjust the tip and tilt of the lens to match the orientation of the chamber window. The lens is also mounted on linear translation stages to align precisely to the ion chain. After the PhotonGear lens, the light is focused and then reimaged using a combination of a Special Optics compound lens (54-17-29-370 nm) and a pair of Thorlabs lenses (LB1294-A and LA4102-UV). This combination yields the desired 125/4.5 magnification for the ion light, with a final spot size of 2- $\mu$ m radius per ion, which can easily couple into a 50- $\mu$ m-diameter multimode fiber core. With this arrangement, we achieve 12 counts per 350  $\mu$ s from a  $^{171}\text{Yb}^+$  ion on resonance, for an estimated total photon collection efficiency of 4e-3 [30].

#### A. DETECTION CROSSTALK

To determine the detection crosstalk of our system, we trap a single ion and measure the photons (or counts) on the PMTs connected to neighboring fiber cores. We Doppler cool the ion for 1 ms, optically pump for 10  $\mu$ s, as described in Section III, perform a  $\pi$ -pulse using microwaves and then detect for 350  $\mu$ s. The light was collected into three PMTs, shown in Fig. 22: one connected to the fiber core centered on the ion (core 2) and one connected on each side of the center ion

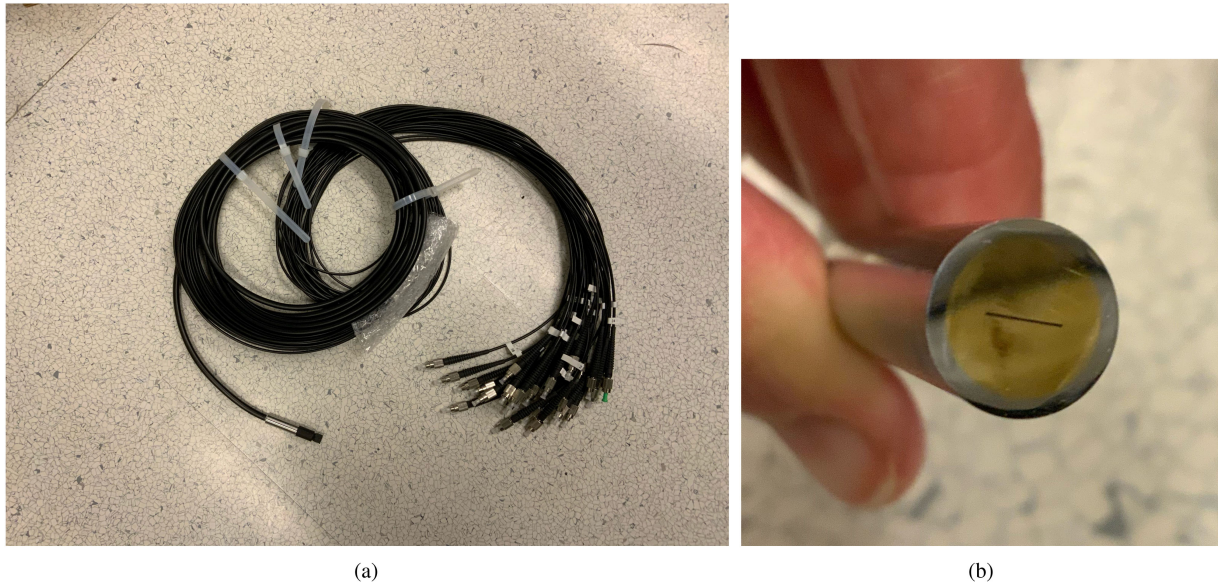


**FIGURE 20.** Multicore fiber allows us to reimaging each ion onto its own fiber and PMT. The result is distinguishable detection with minimal loss and crosstalk. (a) View of the entire single multicore fiber fanning out to 32 individual fibers. These can be easily routed to separate PMTs. (b) View of the multicore fiber tip. The individual cores are indistinguishable in this photo, but the linear arrangement is apparent.

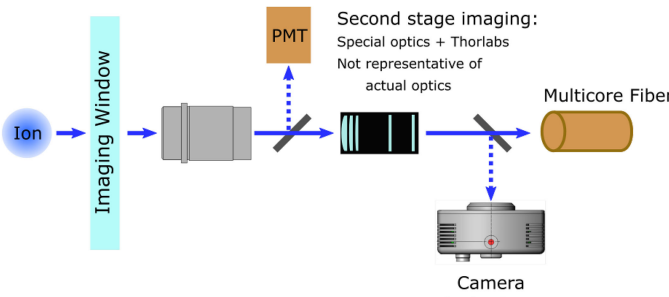


**FIGURE 21.** Schematic of imaging system layout. The motorized flip mirrors deflect the light (dashed arrows) when engaged and pass light straight to the multicore fiber when disengaged. This way, the most sensitive optic is not prone to misalignment by actuating the mirrors.

**TABLE 3.** Results of Detecting a Doppler Cooled Bright Ion on Various Detectors

Counts	Core 1 (no ion)	Core 2 (bright ion)	Core 3 (no ion)
$\leq 1$	100191	991	100161
$> 1$	9	99209	39
Error	1e-4	1e-2	4e-4

In fiber cores 1 and 3, we expect 0 counts and, indeed, only see counts a small fraction of the time. These extraneous counts could be due to light spillover from the bright ion in between the two cores, dark counts from the PMTs, or excess scatter of detection light off the trap. For core 2, the ion was prepared in the bright state. Thus, the fact that the ion is not perfectly bright is representative of a SPAM error, which is accounted for in the listed detection crosstalk error rate.

(cores 1 and 3). We repeat the measurement 100 200 times to look for light leakage from the bright ion on the empty cores. Detecting with a threshold of 1 (0 and 1 counts indicate a dark ion,  $> 1$  count indicates bright), we realize an upper bound of fiber crosstalk error of  $7e-4$  (see Table 3). Since the ion was prepared in state  $|1\rangle$  for detecting the fiber crosstalk, error on the core 2 detection is indicative of a SPAM error. This

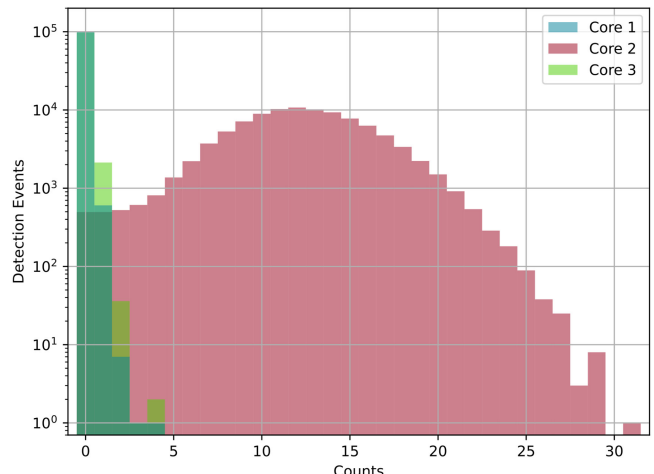


**FIGURE 22.** Detection histogram displaying data from Table 3. Core 2 is centered on the ion, and the corresponding detected events per detected photons show a Poissonian distribution centered at 12 photons (or counts). Cores 1 and 3 are offset from the ion (imaging regions  $4.5 \mu\text{m}$  on either side of the ion) and show mostly 0 count events.

SPAM error is accounted for in the detection crosstalk by subtracting the number of times the bright ion erroneously appeared dark (991) from the total number of dark counts in cores 1 and 3 (100 191 and 100 161, respectively). Dividing the number of bright counts by the adjusted dark counts leads to the errors cited.

## VI. CONTROL HARDWARE

Low-level operation of the experiment, both in its quiescent state and when running experimental sequences, is predominantly controlled via custom field-programmable-gate-array-based circuits. Chief among these circuits are the following:

**TABLE 4.** Single Qubit Gate Fidelities Determined by GST

Parameter	Rotation Angle (°)	Infidelity	$\frac{1}{2}$ -Trace Distance	Sequence Length
Microwave gates				
Bare gates	0.50353 $\pi$	6.86e-4	6.49e-3	2048
BB1 gates	0.49997 $\pi$	3.90e-5	1.78e-4	128
Global Raman Beam				
Bare gate	0.48989 $\pi$	2.11e-3	1.61e-2	1024
BB1 gate	0.49713 $\pi$	6.56e-4	4.69e-3	128
Individual Coprop. Raman Beam				
Bare gates	0.50749 $\pi$	4.10e-3	1.24e-2	1024
BB1 gates	0.50015 $\pi$	1.23e-3	1.70e-3	512

**TABLE 5.** General Settings

Setting	Value
Rf drive	46.888 MHz
Magnetic Field	4.37 G
Doppler Detuning	-13 MHz
Doppler Cooling Duration	1 ms
Detection Time	350 $\mu$ s
Optical Pumping Time	10 $\mu$ s
Sideband Cooling Duration	1.7 ms

- 1) master control system;
- 2) voltage control system;
- 3) coherent control system.

While these boards only comprise a subset of the electronics used throughout the system, they are the key interoperable components that execute timing-critical operations necessary for quantum algorithms.

The master control system's purpose is to orchestrate sequences involving signals that are used to control cw lasers, digital inputs and outputs, and analog inputs and outputs. It is responsible for processes such as loading ions, Doppler cooling, and state detection. Certain steps in experimental sequences require the master control system to lend operational controls a dedicated subsystem, such as the voltage control system used for shuttling ions or the coherent control system for applying gates. Only the coherent control system will be discussed in detail in order to elucidate the low-level pulse control needed to realize quantum gates. While it is not necessary to fully understand the details of the control hardware to run successful circuits on the QSCOUT, our reasons for providing these details to the interested user and scientific community are twofold. First, one of the goals of the QSCOUT is transparency and offering low-level access. Second, a deeper understanding of the inner workings of certain details of the control hardware will help elucidate specific pulse construction requirements [56], in particular global phase synchronization (see Section VI-A1) and frame rotations (see Section VI-A3).

## A. COHERENT CONTROL SYSTEM

The coherent control system uses a custom design, referred to as "Octet," implemented on a Xilinx RFSoC. It is responsible for generating the rf tones that drive the multichannel AOM. Due to the nature of the pulsed laser system, the control electronics satisfy the following requirements:

- 1) radio frequencies ranging from 0 to 409.6 MHz;
- 2) two tones per output channel;

- 3) full waveform generation in the digital domain;
- 4) global phase synchronization;
- 5) gate sequencer, which does the following:
  - 1) schedules pulse sequences used to realize gates;
  - 2) provides simultaneous control over frequency, phase, amplitude, and virtual Z-rotations for all tones and channels. All parameters support discrete and smooth modulation using an on-chip spline interpolator [57];
  - 3) dynamic correction for certain imperfections in the experimental hardware including the following:
    - a) frequency feedback to account for pulsed-laser cavity drift;
    - b) crosstalk cancellation that adds output signals to nearest- and next-nearest-neighbor channels with tunable amplitude and delay.

The details of these features and how they are used for pulse-level control differ from other standard rf delivery systems. While many of these elements are separately optimized and are not exposed to the end user, several features are directly accessible. Knowledge of how they work is vital to understanding how to write custom gates at the pulse level. The latter features and how they are controlled are broken into separate categories.

### 1) GLOBAL PHASE SYNCHRONIZATION

One of the main challenges of coherent control is the ability to have *absolute* control over the rf phase. However, in most systems, this is difficult; it either requires several independent frequency sources that are separately mixed or a lot of manual phase bookkeeping. Using multiple frequency sources and mixing them externally does not scale well, and undesired phase shifts from changes in amplitude and frequency complicate calibration routines. Manual phase bookkeeping allows one to repurpose synthesizers by changing their frequency output. However, this comes with additional challenges and can add computational and data overhead.

A direct digital synthesizer (DDS) can be represented as three main pieces: a phase accumulator,<sup>1</sup> a separate summer for shifting the phase accumulator output by a fixed phase value, and a lookup table (LUT) to convert the phase to a sinusoidal amplitude, as shown in Fig. 23. In the case where

<sup>1</sup>The accumulator is represented as a summer with the output fed back into the second input. It should be assumed that all components are clocked.

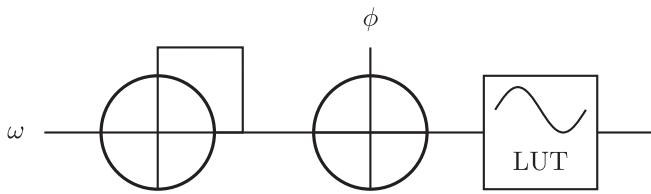


**FIGURE 23.** Diagram highlights the key elements for a simplified model of a DDS. The first component is a phase accumulator, which is represented as a summer that adds a frequency word,  $\omega$ , to the current output on each clock cycle (clock stimulus not shown). This is followed by a dedicated summer for changing the overall phase offset and a LUT that converts the final phase value to a digitized sinusoidal amplitude.

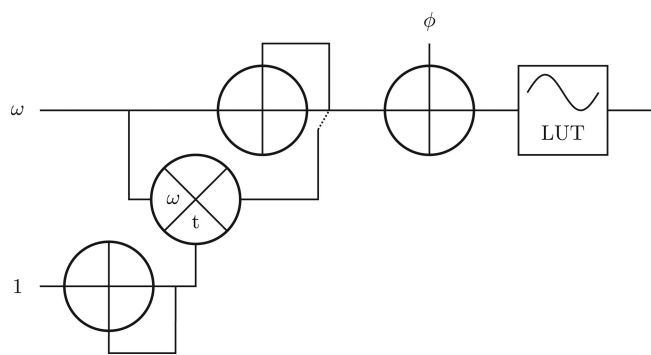


**FIGURE 24.** Modified form of the simplified DDS. A free-running counter tracks the global time,  $t$ , is constantly multiplied against the current frequency word,  $\omega$ , to calculate the global phase,  $\phi' = \omega t$ . The global synchronization operation activates the switch at the output of the phase accumulator for a single clock cycle in order to overwrite the accumulated phase with the global phase.

manual bookkeeping is used, either the external phase input,  $\phi$ , needs to be updated to rotate the phase accumulator output such that it is phase aligned to an earlier point in time after a frequency update or the accumulator needs to be reset to a specific precalculated value.

In the QSCOUT Octet system, phase synchronization is handled using a separate paradigm, in which a global phase is constantly being calculated on chip, as shown in Fig. 24. In this case, a counter (represented as an accumulator with a unity frequency word) is multiplied by the DDS frequency word and updated on every clock cycle. This counter then tracks the global phase for any given frequency by calculating  $\phi' = \omega t$  such that the global phase is zero when  $t = 0$  regardless of frequency. Once a new frequency is applied, the accumulator can be aligned to the global phase for this frequency by overwriting the accumulator output with this global phase. This simply requires sending a “synchronization pulse” that toggles the switch at the accumulator output for a single clock cycle. Although they are not shown in Fig. 24, delay lines have been added at the appropriate places such that a simultaneous update of the frequency word and an application of a synchronization pulse will yield the global phase for the new frequency.

While each Octet board contains 16 custom DDS modules, resulting in eight output channels each comprising two tones,

there is only a single global counter common to all DDSs. This counter is effectively nulled when the board is power cycled and initialized. Thus, no assumptions should be made about the absolute value of the global counter. Proper usage of the synchronization mechanism requires that *every* pulse for which the rf frequency and phase are reused should be applied with a synchronization operation. The absolute phase of the first pulse is effectively random in this case, as it depends on the value of the global counter. As long as the first pulse is synchronized, the phase of the Bloch vector will be set relative to the global phase. Subsequent pulses, for which phase synchronization is also applied, are guaranteed to be properly phase aligned not only to earlier pulses at the same frequency, but the phase alignment is identical across all tones and channels. This is particularly important for the two-qubit MS gates [see Fig. 25(a)], in which the red and blue sideband frequencies form a beat note.

In this case, the global phase of the MS gate is set by the relationship between the phase of the beat note and the phase of the frequency resonant with the qubit transition. Because the QSCOUT system qubit laser drives Raman transitions, any single transition is driven via a beat note given by the difference frequency of the two legs of the Raman transition. This means the two-qubit gate picture is in reality a bit more complex, as shown in Fig. 25(b), and the phase of the beat note between the red and blue sidebands determines the global phase of the MS gate.

Fortunately, this imposes the requirement that the beat note formed by the sidebands needs to be phase aligned only to the relevant leg of the Raman transition. This alignment is easily achieved by using the built-in phase synchronization on the desired tones. However, one of the caveats when working with any type of digital hardware is discretization effects, which can lead to subtle rounding errors because the frequency is limited to a depth of 40 bits. The frequency word,  $F$ , which is sent to the hardware, is converted from a given frequency,  $v$ , by

$$F(v) = \text{round}(v/f_s \times 2^{40}) \quad (1)$$

where  $f_s \equiv 819.2\text{MHz}$  is the effective sampling rate of the DDS. The final value sent to the hardware is rounded to the nearest integer.

These rounding errors can play a larger role when the secondary beat note is involved. For example, the beat frequency generated by the sideband tones is given by

$$\begin{aligned} f(t) &= \sin(\omega_b t + \phi_b) \sin(\omega_r t + \phi_r) \\ &= \frac{1}{2} [\cos((\omega_b - \omega_r)t + \phi_b - \phi_r) \\ &\quad - \cos((\omega_b + \omega_r)t + \phi_b + \phi_r)] \end{aligned} \quad (2)$$

where  $\omega_b$  ( $\omega_r$ ) is the angular frequency of the applied blue (red) sideband, and  $\phi_b$  ( $\phi_r$ ) is the corresponding phase. These frequencies must obey the following condition for proper

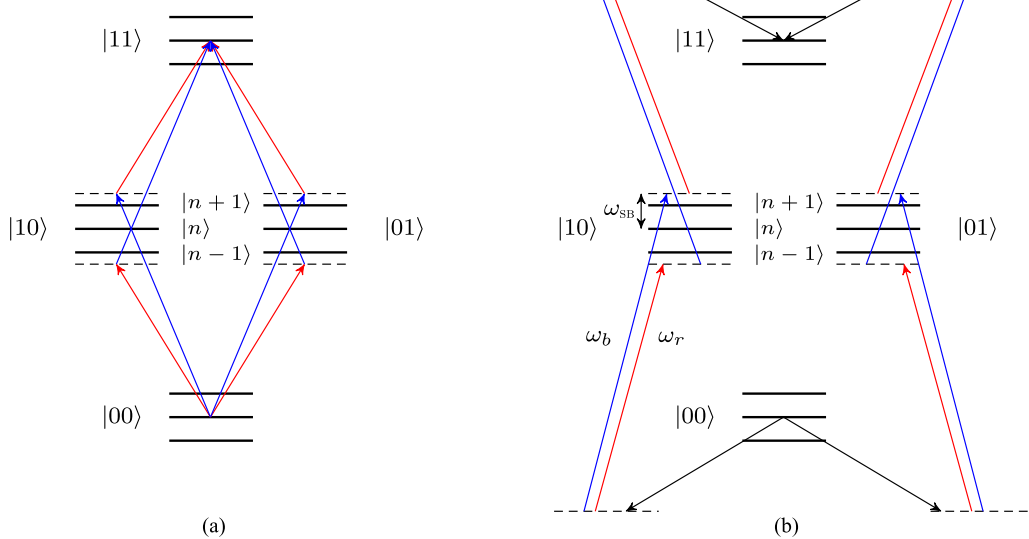


**FIGURE 25.** Diagram of red (red arrows) and blue (blue arrows) sideband transitions used in a two-qubit Mølmer–Sørensen gate.  $|n\rangle$  refers to the number of phonons in a particular motional mode and is the initial phonon number. (a) In the typical model, the red and blue sidebands are directly detuned from the motional sideband transitions and form a beat frequency. The phase of this beat note determines the overall phase of the MS gate. (b) When using Raman beams, the red and blue sideband transitions occur through a virtual state, and in practice, there are three phases involved in determining the MS gate phase. In particular, the beatnote between the red sideband and the “center” (black arrows) frequency form a phase as does the beatnote between the blue sideband and the center frequency. Typically, when finding the overall gate phase, the center frequency cancels out, and only the relative phase between the red and blue sidebands determines the gate phase as in (a). However, machine rounding errors in the frequencies of the red and blue sidebands can lead to discrepancies in this phase if not handled appropriately.

phase alignment:

$$2\omega_{\text{carrier}} = \omega_b + \omega_r. \quad (3)$$

We can define  $\omega_b \equiv \omega_{\text{carrier}} + \omega_{\text{SB}}$  and  $\omega_r \equiv \omega_{\text{carrier}} - \omega_{\text{SB}}$ , and, as an example case, assign them the following values:

$$\begin{aligned} \omega_{\text{carrier}} &= 2\pi \times 228732824.32571054 \text{s}^{-1} \\ \omega_{\text{SB}} &= 2\pi \times 2235174.1793751717 \text{s}^{-1}. \end{aligned} \quad (4)$$

We then use (1) to convert these angular frequencies to the discretized carrier,  $F_{\text{carrier}}$ , red sideband,  $F_r$ , and blue sideband,  $F_b$ , frequencies

$$\begin{aligned} F_{\text{carrier}} &= \text{round}\left(\frac{\omega_{\text{carrier}}}{2\pi f_s} \times 2^{40}\right) &= 307000000000 \\ F_r &= \text{round}\left(\frac{(\omega_{\text{carrier}} - \omega_{\text{SB}})}{2\pi f_s} \times 2^{40}\right) &= 304000000000 \\ F_b &= \text{round}\left(\frac{(\omega_{\text{carrier}} + \omega_{\text{SB}})}{2\pi f_s} \times 2^{40}\right) &= 310000000001. \end{aligned}$$

Unfortunately, for the discretized frequencies, (3) is no longer true, and instead, the two terms differ by one frequency epsilon,  $f_{\text{eps}} \equiv f_s/2^{40} \approx 745 \mu\text{Hz}$ . This is because the discretization is performed *after* calculating the red and blue sideband frequencies ( $\omega_r$  and  $\omega_b$ ). While the frequency offset is small, the resulting phase then differs by  $f_{\text{eps}}(t - t_0)$ , where  $t_0$  is arbitrary, leading to a large, unintended phase shift when applying phase synchronization. This large error can

be avoided by ensuring that (3) is valid in the digital domain before applying phase synchronization.

## 2) FREQUENCY FEEDBACK

Drift in the cavity length of the pulsed laser that is used for driving quantum transitions is not actively corrected at the source. Instead, we use a scheme similar to [58] to correct for frequency errors by feeding forward frequency corrections due to variations in the laser’s repetition rate. Variation in the repetition rate leads to a “breathing” of the frequency comb that is generated by the pulsed laser. In order to bridge the 12.642-GHz qubit transition, the frequency difference between the Raman beams is set such that the closest *integer harmonic* is shifted into resonance with the qubit transition. This means that the frequency error due to variations in the repetition rate must be amplified to account for the net frequency deviation at the target harmonic.

Details of how the repetition rate signal is monitored and converted into a useable signal for locking is described in Section IV-B. This signal is passed into the RFSoC via one of the fast ADC inputs integrated on the chip. The frequency lock involves a complex mixing stage between the ADC data and a dedicated DDS core in the firmware design. The mixed output is sent to a proportional-integral-derivative (PID) module that feeds the error back onto the dedicated DDS to create a phase-locked loop that tracks the repetition rate. The accumulated error is then *optionally* forwarded to the various output tones and subsequently multiplied by the

appropriate harmonic, depending on the specific details of the coherent operation or gate being applied. Different locking configurations arise because the feedforward correction must add a *relative* shift to the tones that are used to realize the Raman transition. In other words, one tone must be shifted by an additional amount to keep the frequency offset of the desired harmonic fixed relative to the other Raman beam. The feedforward correction differs in sign, depending on which leg of the Raman transition the correction is being applied.

Since the correction depends on the integer harmonic and its sign, both of which are not dynamically configurable on a per-gate basis, the user need not worry about the specific details of the underlying lock settings. It is instead more important to consider when the feedforward correction should be applied and to which tones. There are two basic rules of thumb the user should follow.

- 1) Each Raman transition consists of two tones, where exactly one of those tones should have a feedforward correction applied.
- 2) The feedforward correction is applied to the higher frequency tone.

Following the above conventions, frequency feedback for single qubit rotations is straightforward. Whichever tone is higher in frequency receives the feedback, regardless of whether it is copropagating or counterpropagating. However, for the MS gate, red and blue sideband frequencies could be defined around  $f_{\text{upper}}$ , and thus, the frequency feedback should be applied to both tones (meanwhile, a counterpropagating global beam has a single lower frequency with no feedback). Conversely, the sidebands could be defined around  $f_{\text{lower}}$ , in which case  $f_{\text{upper}}$  (as well as the feedforward correction) would be applied to the global beam channel. However, other, more complicated configurations of the MS gate exist [59] that impose different requirements on the lock parameters. These can be handled by frequency locking the two Raman transitions to different harmonics of the frequency comb, which is possible using this hardware.

### 3) FRAME ROTATIONS

Virtual Z-rotations are referred to as “frame rotations,” since the functionality depends on the particular basis for the system. The “frame” nomenclature is used in the design simply for extensibility to future systems. Frame rotations work on the same footing as the phase parameter, except that the phase values are accumulated such that all subsequent gates have an additional phase offset determined by the value in the frame rotation accumulator. Thus, virtual Z-gates are realized by simply adding a phase offset to all subsequent gates, without the need for manual phase bookkeeping. This phase offset can be defined within another gate or they can be a standalone operation. A standalone operation requires a minimum of four clock cycles, roughly 9.77 ns, to prevent underflows in a gate sequence.

Because the frame rotations are specific to the frame of the qubit itself, different configurations are required for how this phase is applied. For example, the phase of a single-qubit gate is determined by a phase difference between the two legs of the Raman transition. Applying a positive phase,  $\phi$ , to the tone used for  $f_{\text{upper}}$  is equivalent to applying  $-\phi$  to  $f_{\text{lower}}$ . However, applying  $\phi$  to both  $f_{\text{upper}}$  and  $f_{\text{lower}}$  will result in an overall phase shift of zero.

Copropagating gates must have the virtual Z-phase forwarded to the appropriate tone and may require a change in sign. On the other hand, the virtual Z-phase will only be correct for an MS gate if the phase is forwarded to *both* tones. Moreover, in alternate configurations, the sign of this phase might need to be inverted on one or both tones. This functionality is handled at the hardware level, where the user only needs to specify which tones should have the virtual phase applied, and for which tones the phase should be inverted.

### 4) GATE SEQUENCER

The Octet design contains two separate modes of operation, which we refer to as *static* and *dynamic*. These modes are not mutually exclusive and are always running at the same time from the perspective of the DDS module. In other words, the DDS is always taking into account separate inputs corresponding to both modes and constantly combining the various input parameters based on their type. Static mode is meant for slow updates, where output channels can be set to a specific frequency, phase, and amplitude with an overall scale factor. Static mode also includes settings for the frequency feedforward target harmonic and crosstalk compensation settings (see Section VI-A5). These settings, which are not exposed to the end user, are primarily used for other experimental operations, such as to assist with ionization when loading ions or adding slow drift corrections.

Dynamic mode is designed for running time-critical sequences of pulses that are used to realize quantum gates. The final static and dynamic values for frequency, phase, and amplitude are simply added together, and the overall scale factor reduces the overall amplitude, each at the hardware level. However, the user should assume that the static mode settings are all zero, except for a unity overall amplitude scaling.

Dynamic mode uses a firmware module, referred to as the “Gate Sequencer,” that is fitted with fast LUTs for recycling pulse data and a set of spline interpolation modules (or “spline engines”) for carrying out parameter modulation. The spline interpolation scheme is based on a NIST design [57] which maps the spline coefficients such that the interpolator can be modeled as a chain of accumulators. This method uses third-order polynomial B-splines or 1-D cubic splines.

The Octet uses spline engines for frequency, phase, amplitude, and frame rotations for both tones on all channels. Because each set of coefficients is calculated for a precise number of time steps or clock cycles, each set of coefficients, as well as the number of clock cycles, is sent as a single word

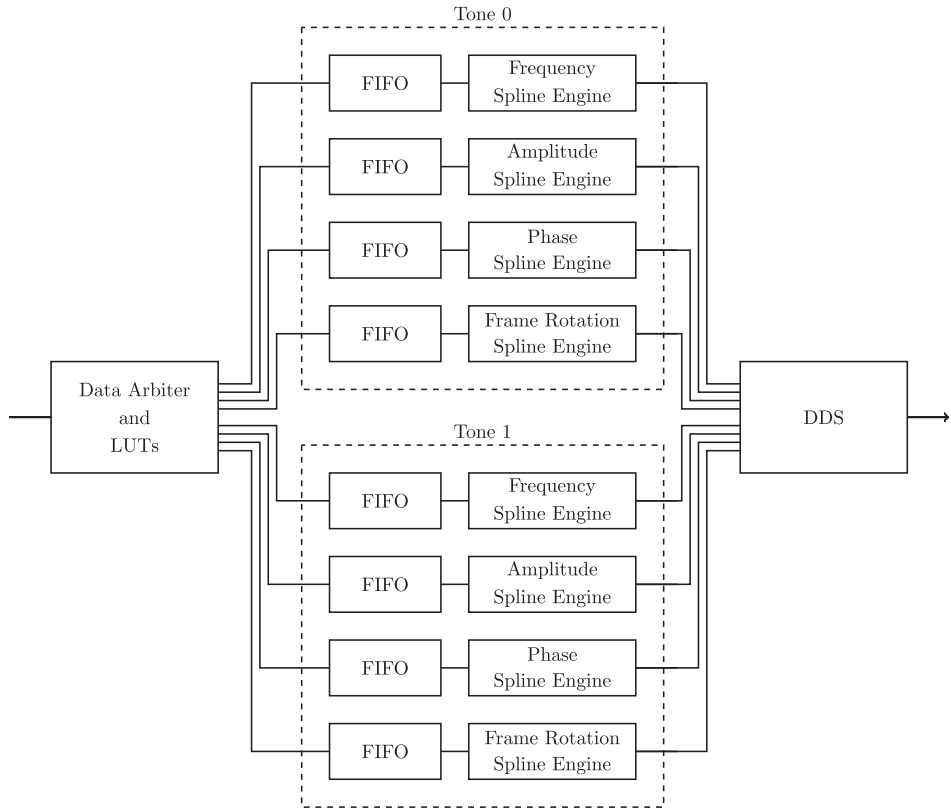


**FIGURE 26.** Gate sequencer spline engine layout. Each parameter has a dedicated spline engine, each of which is fed by a 256 deep FIFO. Incoming data for the particular channel are routed through a data arbitration module and a series of LUTs for recycling data.

to the hardware. Each word contains four 40-bit coefficients,<sup>2</sup> a 40-bit duration, and various other metadata bits used for controlling extra operations, such as phase synchronization, internal routing, and programming information. For uniformity, and to match natural bus widths in the design, the total word size is 256 bits. It has the same format for all spline engines.

Each output channel has a dedicated gate sequencer module, each of which contains a data arbitration module, fast LUTs, and eight spline engines with first-in first-out (FIFO) buffers, as shown in Fig. 26.

Incoming data fill the FIFOs until the gate sequence is either exhausted or the FIFOs are completely filled and present a blocking condition. An external trigger simultaneously enables all spline engines, which will consume data until the FIFOs are empty or a *wait for trigger* flag is encountered in the metadata, at which point the spline engines will wait for another external trigger.

Because each data word carries its own timing information, each spline engine can consume data at different rates

and runs independently from other spline engines. As a result, the number of spline knots per parameter for a given pulse need not match. Rather the total sum of the duration arguments for each parameter should match at the gate level or, in the most extreme case, match the total elapsed timing between *wait for trigger* flags. Asymmetry between the numbers of spline points mainly imposes additional requirements on the order in which the data are sent. This is done in such a way that FIFO blocking for one parameter does not starve another FIFO. This situation is avoided by properly interleaving data based on parameter type and time-sorting data. Each output channel has a dedicated gate sequencer, where each gate sequencer is fed from a common arbiter. It has a structure almost identical to Fig. 26, except that the spline engines would be replaced with gate sequencers, and each gate sequencer feeds a separate DDS. Ultimately, eight channels, each with eight parameters, have to be run simultaneously. They are, however, fed serially. Thus, blocking conditions can arise from parameter FIFOs *and* channel FIFOs. The data sorting must also take into account ordering of all 64 parameter FIFOs across channels.

The overall model requires that *all* spline engines are consuming data during a circuit, even if the data are equivalent to a NOP (no operation), so that data are properly aligned at a later time when the value is potentially nonzero. Specific channels and parameters can, in fact, be disabled to reduce

<sup>2</sup>The 40-bit coefficient size is used since the frequency, phase, and frame rotation word size is 40 bits. However, the 16-bit amplitude words are zero-padded for uniform data size and to allow for additional precision in higher order coefficients, where the least significant bits eventually accumulate. This accumulated error is less of a problem for the 40-bit coefficients because the accumulated error is a part in  $2^{40}$  as opposed to a part in  $2^{16}$ .

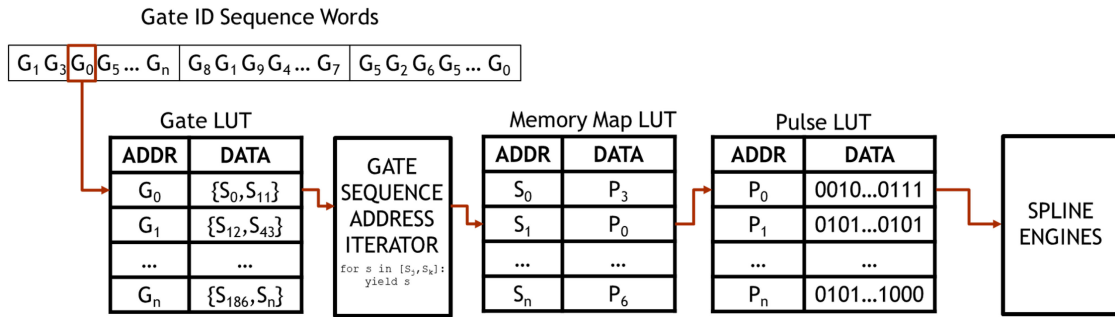


**FIGURE 27.** Gate sequencer LUT layout. Incoming words are, depending on metadata, optionally routed through a cascade of LUTs for reading out the associated pulse data on all parameters and subsequently routed to the correct spline engine input FIFO. Gate IDs can be densely packed in single words to improve overall throughput. These IDs are passed through an initial table to determine the memory bounds that need to be iterated over in a secondary LUT, which provides the final address associated with the final raw pulse data LUT.

overall data for smaller circuits and calibration routines, but this is generally not needed or used. Ignoring potential optimizations, at least one word for each parameter must be provided to describe a gate, which is a minimum of 2 kb of data per gate. This amount of data can add up for long datasets, where latency between circuits needs to be minimal. For an exhaustive protocol such as gate set tomography (GST) [60], the total number of gates used can easily be on the order of  $10^6$ , and with experimental averages and sideband cooling taken into account, the total amount of data associated with even the most simple gates can easily exceed 1 GB. However, since the same basic set of gates is used, streaming the full data for each gate adds a lot of unnecessary overhead. Instead, the gate sequencer implements a series of LUTs (see Fig. 27) to store relevant pulse information for various gates.

The “Pulse LUT” (PLUT) contains raw data words, such as those used in the streaming case, that need to be forwarded to a particular spline engine FIFO. However, a particular gate may contain a large number of PLUT entries, which all need to be sent out to their respective FIFOs. Moreover, two gates might have common PLUT entries, and to reduce overall memory usage, all PLUT entries are generally unique. For example, a simple square pulse X-gate will contain eight data words, but the equivalent type of Y-gate will be identical with the exception of a single phase word; thus, a total of nine PLUT entries are needed to describe both gates. Because PLUT entries are unique and often shared among different gates, a secondary “Memory Map LUT” (MLUT) is used to create dense arrays of pointers in a linear address space. In other words, stepping through a particular set of MLUT addresses will return a series of address words of the PLUT entries needed to describe a particular gate. Gates are then encoded using a set of MLUT address boundaries, packed into a single data word and stored in the “Gate LUT” (GLUT), the output of which is connected to an iterator module for reading out a sequence of MLUT addresses. The GLUT address size is currently set to 6 bits, but it can easily be reconfigured in firmware, and sets the ultimate compression ratio for the data and an upper bound on the number of unique gates that can

be stored locally. Data still must be sent in 256-bit words and, because of metadata constraints, the number of 6-bit GLUT address words, or “gate IDs,” which can be packed into a 256-bit word is 36. This gives a compression ratio of  $\approx 0.35\%$ , neglecting the size of the data used to initially set the LUTs.

While it may seem that the additional overhead for programming the LUTs may, in some cases, encumber the data flow because of additional words needed to program the LUTs, the LUT approach can artificially increase FIFO depths and offers more flexibility. Because programming data and sequence data can be packed into single 256-bit transfers, the total number of data words to program and stream a simple square pulse gate is  $8 + 1 + 1 + 1 = 11$ , where the GLUT, MLUT, and gate ID sequence require one word each. However, there is no requirement that a gate entry incorporates all parameters for a pulse. For example, a frequency-modulated gate could be defined with a fixed amplitude, phase, frame rotation, and tone 0 frequency. The tone 1 frequencies could then be streamed directly after passing in the appropriate gate ID. Additional gains come into play for large amounts of data, where LUTs are programmed at roughly the same update rate of the spline interpolation.<sup>3</sup> Hence, active use of the LUTs might have some additional data, but locally storing sequences in the LUTs can effectively expand the FIFO depth and offers additional gains if data can be partially recycled. Another advantage of this method deals with the fact that data have to cross clock domains via a direct memory access transfer, going from 300 to 409.6 MHz. Since the data are being transferred serially to the 300-MHz clock-domain-crossing FIFOs for eight different channels, the effective frequency for feeding raw data on a single channel is  $(300\text{MHz})/8 = 37.5\text{MHz}$ , which sets the maximum rate at which we can stream data into the fabric. Because the other channels need to be padded with NOPs, this leads to a total time of  $\approx 213\text{ns}$  to stream in a single

<sup>3</sup>The LUTs operate on the 409.6-MHz clock domain, and data words are consumed at different rates depending on the type of programming data and the density of data packed into each programming word.

gate without using the LUTs for data compression. Using the LUTs, thus minimizing FIFO filling on the 300-MHz domain and maximizing the amount of data on the 409.6-MHz domain, will reduce potential data underflow conditions associated with fast spline operations or short gates.

The maximum LUT size is determined by constraints in the fabric and is dominated by the PLUT, which contains  $2^{10}$  entries per channel, while the MLUT contains  $2^{12}$  entries, and the GLUT contains  $2^6$ . Exceeding allocated LUT memory, such as when gates are defined by a large number of unique spline knots, requires either using a combination of directly streamed data with stored data or partially reprogramming of the LUTs between gates. The latter has certain advantages owing to the clock domain crossings, where the buffer FIFOs (see Fig. 27) before the spline engines can store up to 256 words each.

## 5) CROSSTALK COMPENSATION

Crosstalk effects induce undesirable rotations on nearest or next-nearest-neighbor qubits, and they can arise as a result of several possible sources. Optical crosstalk can arise from larger individual addressing beam waists in which a small proportion of stray light is incident on the ions. Other sources of crosstalk are due to unintended driving of neighboring AOM channels, either from electrical crosstalk between transducers or from sympathetic vibrations between crystals. Compensating for these effects requires applying cancellation tones on nearest- and next-nearest-neighbor channels. Cancellation tones need to match the waveforms applied to the neighboring channels, but with a reduced amplitude and, for electrical or acoustic crosstalk, a delay.

To prevent frequency- and amplitude-dependent phase shifts associated with external rf components, crosstalk signals are added digitally in firmware. Coarse delays are, thus, resolution limited by the 409.6-MHz clock used to transfer data. However, fine-tuning the delay can be approximated by applying an overall phase shift to the neighboring output before it is added onto the target channel's waveform. Multiplying the waveform data in the complex domain gives full control over relative phase and amplitude.

Crosstalk compensation *could* be implemented to support infinite feedback, where the output of one DDS channel is added to its neighbor, and the modified output from the neighbor is added back into the original channel *ad infinitum*. This implementation has some advantages, in the sense that it can be used to compensate crosstalk compensation signals themselves. In other words, the compensation signal applied to channel 5 that accounts for the output on channel 7 can be further echoed to channel 3, which is compensating for the output on channel 5. The downside of this approach is that the implicit delay is bounded by the latency of the digital signal processing (DSP) elements in the design that are used to scale and add signals from neighboring channels. Instead, the initial version of the Octet design only applies signals from the *uncompensated* outputs onto neighboring channels. The uncompensated signals are passed into a delay line to match

the latency of the DSP elements that are used to scale and add the compensation signals coming from neighboring channels. This allows for optical crosstalk compensation, where the compensation signals must be perfectly synchronous with the original signal.

## VII. PERFORMANCE

The previous sections outlined the hardware and design decisions that went into the QSCOUT. Here, we discuss some of the experiments where we tested the performance of the overall system. These experiments were performed on either one or two ions.

### A. COHERENCE TIMES

Ions are generally known for their long coherence times, and the QSCOUT system is no exception. Coherence times are typically limited by such factors as the reference clock, external magnetic fields, and noise (from vibrations and power supplies). Fortunately, since we are using a hyperfine qubit and Raman transitions, we are less sensitive to overall phase noise than an ion that has qubit states separated by an optical transition [61]. To reduce the impacts of these factors, this experiment uses an ultrastable Cesium clock CsIII Model 4310B from Microchip with a TSC 4145C OP01 quartz ultra clean-up oscillator to provide a reference 10 MHz to all of our hardware. The specified drift is  $3\text{e-}13$  from 1 to 100 s [62], [63], which allows our microwave coherence times to be long enough that they are limited by ion heating on our current trap devices. Permanent SmCo magnets in a 3-D printed ring mounted to the chamber produce the external magnetic field. These produce a field strength of approximately 4.37 G at the ions that is fairly insensitive to changes in temperature at  $-0.04\%/\text{K}$  [64]. The optical table is floated to reduce the impact of vibrations from equipment, and our sensitive equipment is run from nonswitching power supplies.

To characterize the coherence time, for each configuration, we performed a Hahn echo experiment [65] to estimate the  $T_2$  time, as well as Ramsey experiments [66] to estimate the  $T_2^*$  time. For the Hahn echo experiments, we consecutively applied a  $\pi/2$ -pulse, wait time,  $\pi$ -pulse, wait time, and a final  $\pi/2$ -pulse of varying phase. The final pulse is varied from 0 to  $4\pi$ , and we fit the ion state projection to a sinusoid and extract the phase contrast [inset of Fig. 28(a)]. We repeat for various wait times and fit to a Gaussian decay to determine our  $T_2$  coherence times. We show an example performed with microwave gates in Fig. 28(a), which provides a measure of the coherence free of laser instabilities. Other examples measured with laser gates are provided in Table 6. As the wait time is increased, the sinusoid contrast should collapse symmetrically about 0.5 probability when coherence is lost. Cases where the sinusoid does not appear symmetric about 0.5 are due to ion heating. In our system, when the ion is hotter, it scatters fewer photons during the detection process and biases our state discrimination toward dark states. As a result, the oscillations from the phase

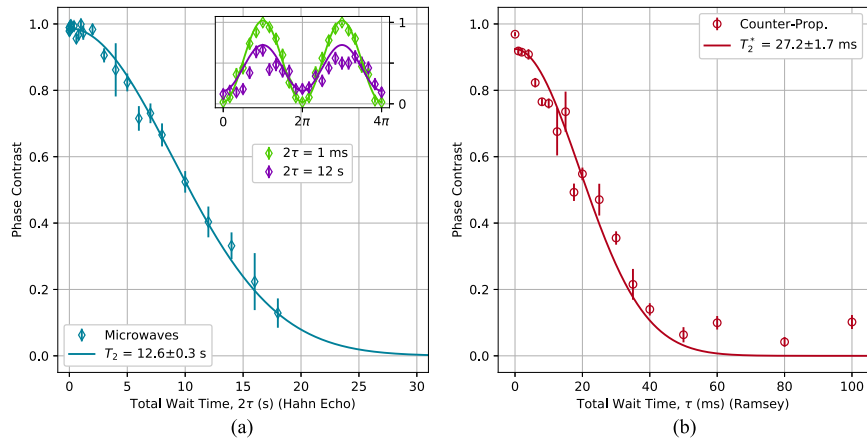


**FIGURE 28.** (a)  $T_2$  coherence measurements taken via a Hahn echo with microwaves reveals a  $T_2$ -time in excess of 10 s (blue). Inset: Phase contrast measurements for two points on the microwave coherence measurement, total wait times of 1 ms (green) and 12 s (purple). The nonsymmetric decay at 12 s indicates ion heating is a limiting factor to the coherence. (b)  $T_2^*$  (Ramsey) coherence measurement using counterpropagating laser beams shows a 27-ms decay.

**TABLE 6.** General Parameters

Parameter	Value	Reference Section
Collision Rate	$3.52 \pm 0.44$ mHz	Sec. II-D
Secular Frequencies (single ion)		
Axial	$0.7 \times 2\pi$ MHz	
Radial 1	$2.1 \times 2\pi$ MHz	
Radial 2	$2.5 \times 2\pi$ MHz	
Principal Axis Rotation	$45^\circ$	
Coherence Times		Sec. VII-A
Microwaves (Hahn Echo)	12.6 s	
Global Raman Beam (Hahn Echo)	11.5 s	
Individual Raman Beam (Hahn Echo)	7.0 s	
Counterprop. Raman Beam (Ramsey)	27 ms	

**TABLE 7.** Infidelities and Errors (Single Qubit, Unless Stated Otherwise)

Parameter	Error	Reference
SPAM	1e-2	
Crosstalk		
Detection	7e-4	Sec. V-A
Coprop. Raman Beams	3e-4	Sec. IV-D1
Counterprop. Raman Beams	4e-2	Sec. IV-D1
Counterprop. Raman Beams with crosstalk comp.	2e-3	Sec. VII-D
Idle Gate	7e-2	
Idle Gate (Compensated)	8e-4	Sec. VII-B
Microwave Gate, bare	6.80e-4	Sec. VII-B
Microwave Gate, BB1	3.9e-5	Sec. VII-B
Raman Beam Single Qubit Gates		
Global, bare	2.11e-3	Sec. VII-B
Global, BB1	6.50e-4	Sec. VII-B
Individual Coprop., bare gates	4.10e-3	Sec. VII-B
Individual Coprop., BB1 gates	1.23e-3	Sec. VII-B
Counterprop., bare gates	not measured	
Counterprop., BB1	not measured	
Z gate	$360^\circ / 2^{40}$ resolution	
Two-Qubit MS gate	2e-2	Sec. VII-E

scans appear centered around a value less than 0.5 [inset of Fig. 28(a)].

The second method for characterizing the coherence times is a pulse sequence of  $\pi/2$ -pulse, wait time, and a final  $\pi/2$ -pulse of varying phase. This sequence is similar to the one used for the Hahn echos, but without the correcting  $\pi$ -pulse to cancel out slow noise or dephasing due to inhomogeneities. In Fig. 28(b), we show the result of this pulse sequence using the counterpropagating beams, which yields

a coherence time  $T_2^*$  of 27 ms, which is sufficient for our target fidelities.

### 1) MICROWAVES

Coherent microwaves can be used to drive the qubit frequency directly. To deliver the microwaves to the ion, we use a microwave horn (Pasternack PE9855/SF-10). This horn is mounted externally to the chamber, and the alignment is

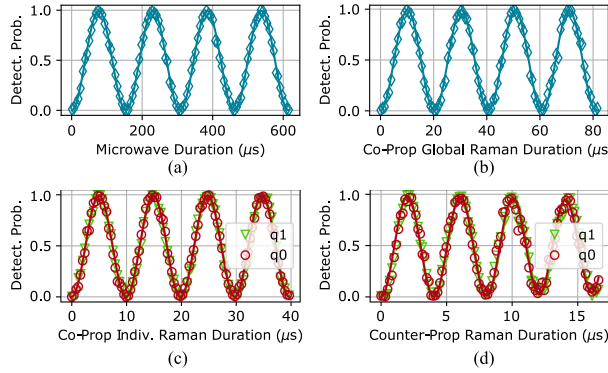


**FIGURE 29.** Typical Rabi oscillations using (a) the microwave horn with a typical  $\pi$ -time of  $80 \mu\text{s}$ , (b) the 355 Raman laser in copropagating global configuration with a typical  $\pi$ -time of  $10 \mu\text{s}$ , (c) the 355 Raman laser in copropagating individual beam configuration with a typical  $\pi$ -time of  $5 \mu\text{s}$ , and (d) the 355 Raman laser in counterpropagating configuration with a typical  $\pi$ -time of  $2 \mu\text{s}$ . Note that the oscillations in (c) and (d), respectively, are performed on two ions simultaneously, and detection is distinguished in their respective fiber cores.

optimized to achieve the highest Rabi frequency. Typical microwave Rabi oscillations are shown in Fig. 29(a).

The microwave frequency is generated by single-sideband modulation of a 12.6-GHz oscillator by an approximately 42.8-MHz signal from the RFSoC (see Section VI), which allows for full frequency, phase, and amplitude control. The detailed description of the microwave frequency generation can be found in [67].

## 2) LASER GATES

Our method for using a pulsed laser to drive Raman transitions for qubit manipulation is described in Section IV. Just as in the case of the microwaves, the phase, frequency, and amplitude of an rf tone applied to an AOM are controlled by the RFSoC. Examples of Rabi oscillations from the 355 laser are shown in Fig. 29. Typical  $\pi$ -times for the Raman transitions are 10, 5, and 2  $\mu\text{s}$  for the copropagating global beam, the copropagating individual beams, and the counterpropagating gates, respectively.

## B. GATE FIDELITIES

Gate fidelities are determined by using GST. This is a characterization method developed at Sandia, which gives a full tomographic description of gates, by performing pulse sequences to efficiently determine errors. For a full explanation of GST, see [67]. For a single ion, GST probes  $G_I$  (the identity gate),  $G_X$  [a  $\pi/2 X$  rotation (phase = 0)],  $G_Y$  [a  $\pi/2 Y$  rotation (phase = 90)]. The implementation of these gates was described in Sections VII-A1 and VII-A2.

Additionally, we implemented GST using BB1 gates for our  $G_X$  and  $G_Y$  rotations, which corrects for pulse length errors [68], [69]. These are a sequence of gates (angle, phase) as follows:  $G(\pi/2, \theta_0) - G(\pi, \theta_1) - G(2\pi, \theta_2) - G(\pi/2, \theta_1)$ , where  $\theta_0$  is the target phase,  $\theta_1 = \theta_0 +$

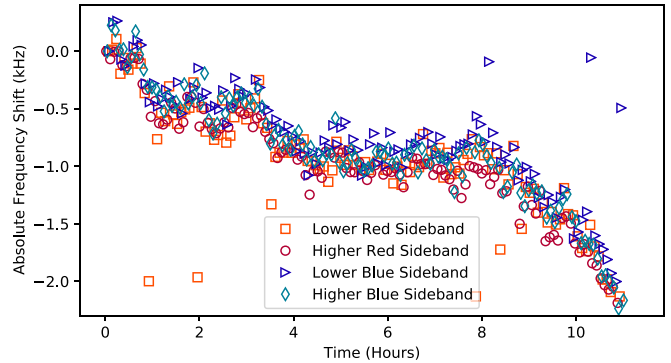


**FIGURE 30.** Measurements of radial secular frequencies for a single ion over the course of  $10+$  h. Both the red and blue sideband of the horizontal and vertical radial modes are tracked. The bandwidth suggests a short-term stability of 200–300 Hz, and a long-term drift of a few kilohertz. These drifts are small enough to achieve our gate fidelity goals.

$\arccos(-1/8)$ , and  $\theta_2 = \theta_0 + 3 \arccos(-1/8)$  (for target angle =  $\pi/2$ ). We also use a modified idle gate, which has a gate time similar to the BB1 compensated gates. The compensated idle gate is a sequence of  $G(\pi, 0) - G(\pi, 90) - G(\pi, 0) - G(\pi, 90)$ .

The results from our gates are compared to an overcomplete basis set from a “black box” model to determine the gate errors. As a result, we get a wealth of information, including gate decompositions, gate error generators, and other traditional fidelity metrics, which can be used to determine the sources of some gate infidelity. A summary of our typical GST result showing gate fidelity and rotations is in Table 4.

## C. RF STABILITY

To achieve consecutive high-fidelity gates, the motional modes of the ion need to be consistent from one gate to the next. The two-qubit gate, in particular, is sensitive to the motional mode frequencies and can suffer fidelity loss if the modes at run time are different from those when the gate was calibrated. Mode drift during the gate will also result in errors, but for now we assume that drift is slower than the timescale of the gates. We track the stability of our radial modes over time to determine the stability of the system (see Fig. 30). Short-term variation ( $\approx 1$  h) is on the order of 200–300 Hz. The long-term drift (several hours to days) is typically a few kilohertz. These drifts are within the range necessary to achieve our experimental goals.

## D. CROSSTALK COMPENSATION

As discussed in Sections IV-D1 and VI-A5, we have the ability to compensate optical crosstalk from a gate being driven on one ion onto its nearest neighbor and next nearest neighbor ion. As a demonstration, we apply a counterpropagating pulse of varying duration on one ion, qubit 0, and measure its effect on its nearest neighbor, qubit 1, sitting  $4.5 \mu\text{m}$  away. For example, as shown in Fig. 31, the power necessary to drive an  $\approx 6 \mu\text{s}$   $\pi$ -pulse on qubit 0, induces an  $\approx 140 \mu\text{s}$

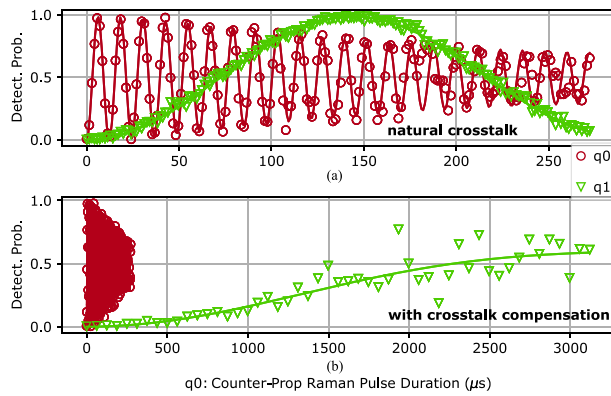


**FIGURE 31.** (a) Rabi oscillations driven on qubit 0 (red) and corresponding natural crosstalk-driven Rabi oscillations seen on qubit 1 (green). Before any crosstalk compensation, Rabi oscillations seen on qubit 1 are about 4.1% of the original signal on qubit 0. (b) After compensation through the Octet hardware (original signal with an amplitude of 0.034 and a phase shift of  $68^\circ$ ), the resultant compensated crosstalk-driven Rabi oscillations seen on qubit 1 are now 0.17% of the original signal on qubit 0. The Rabi oscillation decay is caused by a combination of amplitude and phase fluctuations of the driving laser and finite temperature effects.

$\pi$ -pulse on qubit 1. When we apply a crosstalk compensation on qubit 1, with an amplitude of 0.034 of the original signal on qubit 0 phase-shifted by  $68^\circ$  (found empirically), we measure a resultant  $\pi$ -time of 3.6 ms, or 0.17% crosstalk after compensation.

#### E. TWO-QUBIT GATE

Two-qubit entangling gates are performed using MS gates [46] and shown in Fig. 32. After performing an MS gate, to verify the resultant state is a Bell state, we apply a  $\pi/2$ -pulse of varying phase and measure the state parity  $P_{00} + P_{11} - P_{01} - P_{10}$  [70]. We shape the pulses for the MS gate to have a Gaussian envelope from the RFSoC, which empirically provides a higher fidelity than square pulses.

#### F. MICROMOTION COMPENSATION AND RECALIBRATION

Excess micromotion in this system is compensated using a variety standard techniques, for instance, the “resolved sideband measurement” technique [71], as well as a custom “chirped tickle” (see Section VII-F1) technique. This calibration is done daily and before any user code is run on the system. Since the system is not yet fully automated, recalibration is performed when the operator notices a decrease in gate fidelity. This occurs on the order of a few hours<sup>4</sup> and seems to stem mostly from drifting electric fields moving the ions, so they are no longer centered in the tightly focused laser beams. The recalibration procedure may consist of simply using the voltage on the trap to recenter the ions in the beams. Sometimes, a full recalibration is required, which includes micromotion compensation, measuring the secular

<sup>4</sup>Charging due to photoionization laser scatter or heating effects in some systems may affect compensation; however, we observe no such effects in this system.

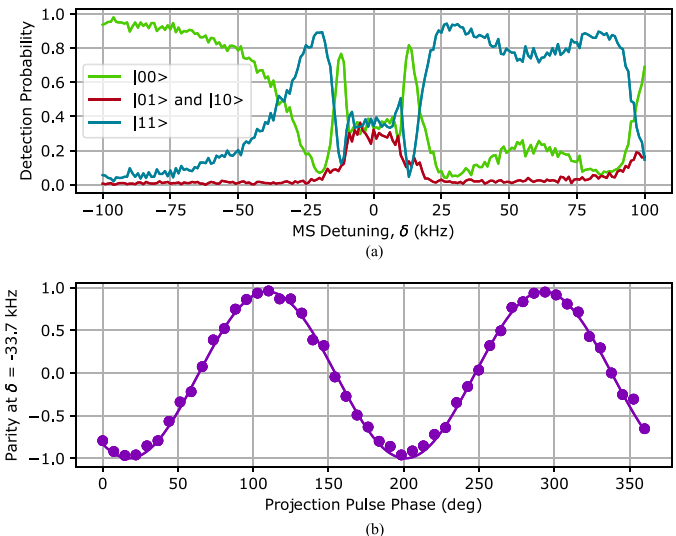


**FIGURE 32.** Mølmer–Sørensen two-qubit gate is performed between two ions. (a) For a pulse duration of  $200\ \mu\text{s}$ , a scan of the detuning from the red and blue sidebands with the populations is shown. The crossing at  $-33.7\ \text{kHz}$  generates the entangled state,  $|00\rangle + |11\rangle$ . The asymmetry of the detuning scan is due to another sideband located  $\approx 120\ \text{kHz}$  away from the sideband used to perform the gate. (b) For a pulse duration of  $200\ \mu\text{s}$  and a detuning of  $-33.7\ \text{kHz}$ , single-qubit projection pulses are then performed and their phase is swept. The parity is calculated from the populations of the different configurations,  $P_{00} + P_{11} - P_{01} - P_{10}$ . An estimated parity of 0.955 suggests an entanglement fidelity of 0.978.

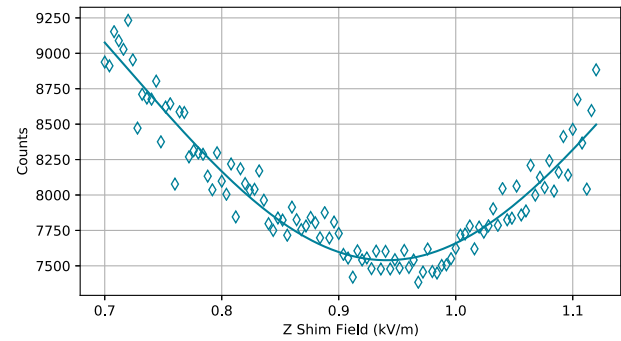


**FIGURE 33.** Ion fluorescence per shim field in the  $\hat{z}$ -direction using the chirped tickle technique. The minimum fluorescence corresponds to the optimum  $\hat{z}$  shim field.

frequencies and measuring the Rabi rates. The procedure can take between 5 and 20 min.

#### 1) CHIRPED TICKLE COMPENSATION

Resolved-sideband micromotion minimization is limited to compensating along directions that overlap with the interrogation lasers. Alternative techniques exist [72], [73], where Doppler-enhanced fluorescence is amplified by parametrically heating motional modes of the ions. This approach requires rotating the principal axes of the confining potential such that they overlap both the axis of the laser used for detection and the micromotion axis to be adjusted, allowing compensation along directions orthogonal to laser beam axes. This technique, however, requires many scans and can

be slow. We use a variation of this technique, which we refer to as “chirped tickle,” which can yield a substantial speedup and calibration times comparable to resolved-sideband micromotion minimization.

Modulating the rf confinement by the secular frequency of one of the off-axis modes will induce a large motional excitation. This excitation can be measured by an increase in ion fluorescence induced by a laser that is sufficiently red-detuned from resonance.<sup>5</sup> Because the motional sideband excitation is proportional to the strength of the rf field at the ion, the amplitude of the micromotion, and thus the measured fluorescence, decreases as the ion approaches the rf null.

In surface-ion traps, anharmonic components of the confining potential are greatest in higher order  $z$ —in our system  $\hat{z}$  is the direction normal to the trap surface and is also perpendicular to our laser beams—terms, particularly for the radial modes which are predominantly set by the rf pseudopotential. Thus, changes in the  $z$ -position strongly couple to the  $zy^2$  and  $z^3$  components of the potential, resulting in  $z$ -dependent frequency shifts of the radial modes. These frequency shifts require the parametric-heating (aka “tickle”) scans to be 2-D, in which the linear shim field along  $\hat{z}$  is adjusted, and then, the rf sideband frequency is scanned to account for the resulting change in secular frequency. This method has the benefit that it allows one to track the motional mode frequency as the  $\hat{z}$  field is changed, but it has the drawback that these scans can be time consuming. In most cases, however, the goal is to simply minimize micromotion regardless of the intermediate or final secular frequencies, especially when doing initial calibrations in a new trap or a new trap region, where the stray fields may slightly differ.

Instead, we use a variation on the 2-D tickle scan, in which we modulate the rf confinement using a frequency chirp. The chirp is implemented via a continuous linear piecewise (triangle wave) frequency modulation, where the bounds are determined by the overall range in secular frequencies we expect to observe while sweeping the  $\hat{z}$  shim field. Typical ramp times are 1 ms for each leg of the chirp, for a total period of 2 ms on the triangle wave modulation. We then detune our Doppler cooling laser by  $\approx 20$  MHz and scan the  $\hat{z}$  shim field. By setting the acquisition time to an integer multiple of the ramp period, we are guaranteed to sample the full frequency range with equal sampling of all frequencies in the chirp.

The experimental step is now reduced to a single 1-D scan of the shim field with only a Doppler cooling stage, during which the ion fluorescence serves as the measurement for each value of the shim field. Each shim field point generally takes 300 ms. In practice, the ramp and acquisition times are generally fixed, and the upper and lower frequency bounds for the chirp as well as the overall amplitude of the modulation are varied to sufficiently excite the mode. For wider scans, parametric heating occurs over a proportionally

smaller range of the chirp, which may require increasing drive amplitude to maintain a favorable signal-to-noise ratio (SNR). If the drive amplitude is too large, the frequency range of the chirp is too small, or the ramp times are too long, the ion can be excited so strongly that it is lost from the trap.

Once a reasonable set of parameters are determined, these “chirped tickle” scans can be performed over wide shim field ranges (several kV/m) for preliminary<sup>6</sup> calibration without ion loss, as well as narrow ranges (1–100 V/m) with larger SNR for final calibration. In each case, the total time for a scan generally takes 1–2 min depending on the number of points. Because the acquisition times are an even multiple of the chirp period, the experimental process is greatly simplified, and the initial phase of the chirp has no impact on the measurement. We use a Tektronix AFG3102 function generator and simply enable the output for the entire duration of the scan. Moreover, initial tuning of parameters and even rough calibrations can be done by manually adjusting the shim fields and simply observing fluorescence, while the chirp is enabled. An example of one of the scan outputs is shown in Fig. 33. Depending on the scan parameters, the resolution of this technique can be  $< 1$  V/m.

Some special considerations must be taken into account when doing a chirped tickle. Insufficient bounds on the chirp can lead to a sharp drop off in the fluorescence signal if the motional mode frequency moves out of this range. Intensity variations of the cooling beam can lead to a background signal that has some curvature, in which case steps may need to be taken to account for background subtraction. Finally, if the range of chirp frequencies is large enough to span the fundamental mode frequency and its harmonics, there can be interference effects depending on the relative phase of the drive frequencies during the chirp. However, using a chirp span that is roughly matched to the expected range of secular frequencies, and keeping the range of shim fields small enough to neglect background curvature associated with the beam profile, this method can easily provide quick calibrations with clean signals.

## VIII. SUMMARY

In summary, this document has outlined the major decisions and implementations to build a quantum processor of up to 32 qubits based on trapped ions. It has created a blueprint for the current QSCOUT machine, with an emphasis on new technologies that enables expanding from one or two qubits to many. In particular, the major new technology introduced in this article is the Octet system for providing frequency feedback, frame rotations, and gate sequencing, which is described in Section VI. Other new technologies include engineering chamber internals to eliminate all organics in the chamber, optical design of 355 laser paths, custom mechanical mounts for sensitive optics, and the chirped tickle micromotion compensation technique. The details included

<sup>5</sup>While the same effect can be observed by a reduction in the ion fluorescence from resonant laser light, we find using a red-detuned beam helps prevent ion loss since the ion is aggressively recooled.

<sup>6</sup>For example, wide ranges are especially useful when calibrating a new trap, but not necessary for daily calibrations.

**TABLE 8.** Approximate Gate Duration

Parameter	Time	Reference
Idle	variable	
Microwave		
Bare gate	80 $\mu$ s	Sec. VII-A1
BB1 gate	720 $\mu$ s	
Global Raman Beam gate		
Bare gate	10 $\mu$ s	Sec. VII-A1, Fig. 29
BB1 gate	90 $\mu$ s	
Individual Coprop. Raman Beam gate		
Bare gate	5 $\mu$ s	Sec. VII-A1, Fig. 29
BB1 gate	45 $\mu$ s	
Counterprop. Raman Beam gates		
Bare gate	2 $\mu$ s	Sec. VII-A1, Fig. 29
BB1 gate	18 $\mu$ s	
Z gate	10 ns	Sec. VI-A3
Two-Qubit MS gate	100-200 $\mu$ s	Sec. VII-E

are to assist QSCOUT users and potential users in evaluating the system for their algorithms, help them tailor programs for best chance of success, and help outside experimental trapped ion groups build their own systems.

## IX. QSCOUT SPECIFICATIONS SUMMARY

Tables 5–8 are included as a reference for the user. They are the QSCOUT specifications, including general settings and parameters, infidelities and errors, and approximate gate durations.

## ACKNOWLEDGMENT

The authors would like to thank Marko Cetina, Alan Bell, Ken Brown, Jungsang Kim, and Bert Tise for many useful discussions. This article describes objective technical results and analysis. Any subjective views or opinions that might be expressed in the article do not necessarily represent the views of the U.S. Department of Energy or the U. S. Government. SAND2021-3837O.

## REFERENCES

- [1] F. Arute *et al.*, “Quantum supremacy using a programmable superconducting processor,” *Nature*, vol. 574, pp. 505–510, 2019, doi: [10.1038/s41586-019-1666-5](https://doi.org/10.1038/s41586-019-1666-5).
- [2] H.-S. Zhong *et al.*, “Quantum computational advantage using photons,” *Science*, vol. 370, pp. 1460–1463, Dec. 2019, doi: [10.1126/science.abe8770](https://doi.org/10.1126/science.abe8770).
- [3] J. Preskill, “Quantum Computing in the NISQ era and beyond,” 2018, *arXiv:1801.00862*.
- [4] IBM Quantum Computing, IBM, Accessed: Mar. 15, 2021. [Online]. Available: <https://www.ibm.com/quantum-computing/>
- [5] Rigetti: Think Quantum, Rigetti Computing, Accessed: Mar. 15, 2021. [Online]. Available: <https://www.rigetti.com/>
- [6] IonQ: The Future is Quantum, IonQ, Accessed: Mar. 15, 2021. [Online]. Available: <https://ionq.com/>
- [7] P. H. Fisk, M. J. Sellars, M. A. Lawn, and G. Coles, “Accurate measurement of the 12.6 GHz clock transition in trapped (171)Yb() ions,” *IEEE Trans Ultrason. Ferroelectr. Freq. Control*, vol. 44, no. 2, pp. 344–354, 1997, doi: [10.1109/58.585119](https://doi.org/10.1109/58.585119).
- [8] Y. Wang *et al.*, “Single-qubit quantum memory exceeding ten-minute coherence time,” *Nature Photon.*, vol. 11, pp. 646–650, 2017, doi: [10.1038/s41566-017-0007-1](https://doi.org/10.1038/s41566-017-0007-1).
- [9] C. J. Ballance, T. P. Harty, N. M. Linke, M. A. Sepiol, and D. M. Lucas, “High-fidelity quantum logic gates using trapped-ion hyperfine qubits,” *Phys. Rev. Lett.*, vol. 117, 2016, Art. no. 060504, doi: [10.1103/PhysRevLett.117.060504](https://doi.org/10.1103/PhysRevLett.117.060504).
- [10] R. Noek *et al.*, “High speed, high fidelity detection of an atomic hyperfine qubit,” *Opt. Lett.*, vol. 38, no. 22, pp. 4735–4738, Nov. 2013, doi: [10.1364/OL.38.004735](https://doi.org/10.1364/OL.38.004735).
- [11] K. A. Landsman *et al.*, “Two-qubit entangling gates within arbitrarily long chains of trapped ions,” *Phys. Rev. A*, vol. 100, Aug. 2019, Art. no. 022332, doi: [10.1103/PhysRevA.100.022332](https://doi.org/10.1103/PhysRevA.100.022332).
- [12] H. Kaufmann *et al.*, “Fast ion swapping for quantum-information processing,” *Phys. Rev. A*, vol. 95, May 2017, Art. no. 052319, doi: [10.1103/PhysRevA.95.052319](https://doi.org/10.1103/PhysRevA.95.052319).
- [13] P. Maunz, “High optical access trap 2.0,” Sandia National Laboratories, Albuquerque, NM, USA, Tech. Rep. SAND2016-0796R, 2016.
- [14] M. G. Blain, R. Haltli, P. Maunz, C. D. Nordquist, M. Revelle, and D. Stick, “Hybrid MEMS-CMOS ion traps for NISQ computing,” *Quantum Sci. Technol.*, vol. 6, 2021, Art. no. 034011, doi: [10.1088/2058-9565/ac01bb](https://doi.org/10.1088/2058-9565/ac01bb).
- [15] R. Islam *et al.*, “Beat note stabilization of mode-locked lasers for quantum information processing,” *Opt. Lett.*, vol. 39, no. 11, pp. 3238–3241, Jun. 2014, doi: [10.1364/OL.39.003238](https://doi.org/10.1364/OL.39.003238).
- [16] A. J. Landahl *et al.*, “Jaql, the quantum assembly language for QSCOUT,” 2020, *arXiv:2003.09382*.
- [17] B. C. A. Morrison *et al.*, “Just another quantum assembly language (Jaql),” in *Proc. IEEE Int. Conf. Quantum Comput. Eng.*, 2020, pp. 402–408, doi: [10.1109/QCE49297.2020.00056](https://doi.org/10.1109/QCE49297.2020.00056).
- [18] G. Pagano *et al.*, “Cryogenic trapped-ion system for large scale quantum simulation,” *Quantum Sci. Technol.*, vol. 4, no. 1, Oct. 2018, Art. no. 014004, doi: [10.1088/2058-9565/aae0fe](https://doi.org/10.1088/2058-9565/aae0fe).
- [19] M. G. House, “Analytic model for electrostatic fields in surface-electrode ion traps,” *Phys. Rev. A*, vol. 78, Sep. 2008, Art. no. 033402, doi: [10.1103/PhysRevA.78.033402](https://doi.org/10.1103/PhysRevA.78.033402).
- [20] M. C. Revelle, “Phoenix and peregrine ion traps,” 2020, *arXiv:2009.02398*.
- [21] Outgassing Data for Selecting Spacecraft Materials System, 2020. [Online]. Available: <https://outgassing.nasa.gov/>
- [22] B. Zajec and V. Nemanić, “Hydrogen bulk states in stainless-steel related to hydrogen release kinetics and associated redistribution phenomena,” *Vacuum*, vol. 61, pp. 447–452, 2001, doi: [10.1016/S0042-207X\(01\)00142-7](https://doi.org/10.1016/S0042-207X(01)00142-7).
- [23] J. A. Fedchak *et al.*, “Outgassing rate comparison of seven geometrically similar vacuum chambers of different materials and heat treatments,” *J. Vac. Sci. Technol. B*, vol. 39, no. 2, 2021, Art. no. 024201, doi: [10.1116/6.00000657](https://doi.org/10.1116/6.00000657).
- [24] Y. T. Sasaki, “A survey of vacuum material cleaning procedures: A subcommittee report of the american vacuum society recommended practices committee,” *J. Vac. Sci. Technol. A*, vol. 9, no. 3, pp. 2025–2035, 1991, doi: [10.1116/1.577449](https://doi.org/10.1116/1.577449).
- [25] G. Chen, “On the physics of purple-plague formation, and the observation of purple plague in ultrasonically-joined gold-aluminum bonds,” *IEEE Trans. Parts Mater. Packag.*, vol. PMP-3, no. 4, pp. 149–153, Dec. 1967, doi: [10.1109/TPMP.1967.1135733](https://doi.org/10.1109/TPMP.1967.1135733).
- [26] B. Selkison and T. A. Longo, “A study of purple plague and its role in integrated circuits,” *Proc. IEEE*, vol. 52, no. 12, pp. 1638–1641, 1964, doi: [10.1109/PROC.1964.3459](https://doi.org/10.1109/PROC.1964.3459).
- [27] J. D. Siversen, L. R. Simkins, S. Weidt, and W. K. Hensinger, “On the application of radio frequency voltages to ion traps via helical resonators,” *Appl. Phys. B*, vol. 107, no. 4, pp. 921–934, Jun. 2012, doi: [10.1007/s00340-011-4837-0](https://doi.org/10.1007/s00340-011-4837-0).

- [28] Ion Gauge Gas Correction Factors, Duniway Stockroom Corp., Fremont, CA, USA, Accessed: Jun. 3, 2021. [Online]. Available: [https://www.duniway.com/images/\\_pg/ion-gauge-gas-correction-factors.pdf](https://www.duniway.com/images/_pg/ion-gauge-gas-correction-factors.pdf)
- [29] Y. Aikyo, G. Vrijen, T. W. Noel, A. Kato, M. K. Ivory, and J. Kim, "Vacuum characterization of a compact room-temperature trapped ion system," *Appl. Phys. Lett.*, vol. 117, no. 23, 2020, Art. no. 234002, doi: [10.1063/5.0029236](https://doi.org/10.1063/5.0029236).
- [30] S. Olmschenk, K. C. Younge, D. L. Moehring, D. N. Matsukevich, P. Maunz, and C. Monroe, "Manipulation and detection of a trapped  $\text{Yb}^+$  hyperfine qubit," *Phys. Rev. A*, vol. 76, 2007, Art. no. 0 52314, doi: [10.1103/PhysRevA.76.052314](https://doi.org/10.1103/PhysRevA.76.052314).
- [31] C. Balzer *et al.*, "Electrodynamically trapped  $\text{Yb}^+$  ions for quantum information processing," *Phys. Rev. A*, vol. 73, 2006, Art. no. 041407(R), doi: [10.1103/PhysRevA.73.041407](https://doi.org/10.1103/PhysRevA.73.041407).
- [32] A. S. Bell, P. Gill, H. A. Klein, and A. P. Levick, "Laser cooling of trapped Ytterbium ions using a four-level optical-excitation scheme," *Phys. Rev. A*, vol. 44, no. 1, 1991, Art. no. R20(R), doi: [10.1103/PhysRevA.44.R20](https://doi.org/10.1103/PhysRevA.44.R20).
- [33] M. Roberts, P. Taylor, G. P. Barwood, P. Gill, H. A. Klein, and W. R. C. Rowley, "Observation of an electric octupole transition in a single ion," *Phys. Rev. Lett.*, vol. 78, no. 10, pp. 1876–1879, 1997, doi: [10.1103/PhysRevLett.78.1876](https://doi.org/10.1103/PhysRevLett.78.1876).
- [34] V. Gerginov, "Time and frequency metrology at PTB: Recent results," Proc. SPIE, vol. 8132, 2011, Art. no. 81320H, doi: [10.1117/12.892675](https://doi.org/10.1117/12.892675).
- [35] A. Ransford, *Personal Communication*, 2019.
- [36] D. J. Larson, J. C. Bergquist, J. J. Bollinger, W. M. Itano, and D. J. Wineland, "Sympathetic cooling of trapped ions: A laser-cooled two-species nonneutral ion plasma," *Phys. Rev. Lett.*, vol. 57, 1986, Art. no. 70, doi: [10.1103/PhysRevLett.57.70](https://doi.org/10.1103/PhysRevLett.57.70).
- [37] R. W. P. Drever *et al.*, "Laser phase and frequency stabilization using an optical resonator," *Appl. Phys. B*, vol. 31, pp. 97–105, 1983, doi: [10.1007/BF00702605](https://doi.org/10.1007/BF00702605).
- [38] E. D. Black, "An introduction to Pound-Drever-Hall laser frequency stabilization," *Amer. J. Phys.*, vol. 69, pp. 79–87, 2001, doi: [10.1119/1.1286663](https://doi.org/10.1119/1.1286663).
- [39] D. R. Leibrandt and J. Heidecker, "An open source digital servo for atomic, molecular, and optical physics experiments," *Rev. Sci. Instrum.*, vol. 86, 2015, Art. no. 123115, doi: [10.1063/1.4938282](https://doi.org/10.1063/1.4938282).
- [40] M. Cetina *et al.*, "Quantum gates on individually-addressed atomic qubits subject to noisy transverse motion," 2020, *arXiv:2007.06768*.
- [41] M. Revelle, C. W. Hogle, B. Ruzic, P. L. W. Maunz, K. Young, and D. Lobser, "Demonstration of sideband cooling on the  $^{171}\text{Yb}^+$  quadrupole transition," Sandia National Laboratories, Albuquerque, NM, USA, Tech. Rep. SAND2019-0668C671715, 2019.
- [42] U. Schünemann, H. Engler, R. Grimm, M. Weidemüller, and M. Zielonkowski, "Simple scheme for tunable frequency offset locking of two lasers," *Rev. Sci. Instrum.*, vol. 70, pp. 242–243, 1999, doi: [10.1063/1.1149573](https://doi.org/10.1063/1.1149573).
- [43] Qubit GmbH, *PM -yb+ -qubit GmbH*, Jan. 2021. [Online]. Available: <https://www.qubit.com/products/electro-optic-modulators-230/phase-modulators/ytterbium-ion.html>
- [44] C. Ospelkaus, C. E. Langer, J. M. Amini, K. R. Brown, D. Leibfried, and D. J. Wineland, "Trapped-ion quantum logic gates based on oscillating magnetic fields," *Phys. Rev. Lett.*, vol. 101, 2008, Art. no. 090502, doi: [10.1103/PhysRevLett.101.090502](https://doi.org/10.1103/PhysRevLett.101.090502).
- [45] D. P. L. A. Craik *et al.*, "Microwave control electrodes for scalable, parallel, single-qubit operations in a surface-electrode ion trap," *App. Phys. B*, vol. 114, pp. 3–10, 2014, doi: [10.1007/s00340-013-5716-7](https://doi.org/10.1007/s00340-013-5716-7).
- [46] K. Mølmer and A. Sørensen, "Multipartite entanglement of hot trapped ions," *Phys. Rev. Lett.*, vol. 82, pp. 1835–1838, 1999, doi: [10.1103/PhysRevLett.82.1835](https://doi.org/10.1103/PhysRevLett.82.1835).
- [47] D. J. Wineland, C. Monroe, W. M. Itano, D. Leibfried, B. E. King, and D. M. Meekhof, "Experimental issues in coherent quantum-state manipulation of trapped atomic ions," *J. Res. Natl. Inst. Stand. Technol.*, vol. 103, pp. 259–328, 1998, doi: [10.6028/jres.103.019](https://doi.org/10.6028/jres.103.019).
- [48] D. Leibfried, R. Blatt, C. Monroe, and D. Wineland, "Quantum dynamics of single trapped ions," *Rev. Mod. Phys.*, vol. 75, pp. 281–324, 2003, doi: [10.1103/RevModPhys.75.281](https://doi.org/10.1103/RevModPhys.75.281).
- [49] Coherent Inc., Paladin compact 355, Dec. 2020. [Online]. Available: <https://www.coherent.com/lasers/laser/paladin-compact-355>
- [50] *L3Harris Technologies*, Acousto optic solutions, Dec. 2020. [Online]. Available: <https://www.l3harris.com/all-capabilities/acousto-optic-solutions>
- [51] S. Debnath, N. M. Linke, C. Figgatt, K. A. Landsman, K. Wright, and C. Monroe, "Demonstration of a small programmable quantum computer with atomic qubits," *Nature*, vol. 536, pp. 63–66, 2016, doi: [10.1038/nature18648](https://doi.org/10.1038/nature18648).
- [52] *OptiCentric* 100: Highly precise lens centering measurement, alignment and assembly systems, Trioptics 2021. [Online]. Available: <https://trioptics.com/wp-content/uploads/2019/09/OptiCentric-100-Brochure-EN-V-002.pdf>
- [53] E. G. Winrow *et al.*, "Ground based, discrete zoom telescope (abridged - optomechanical)," Sandia National Laboratories, Albuquerque, NM, USA, Tech. Rep. SAND2016-8482, 2019.
- [54] *Photon Gear Inc.*, Custom optics, assemblies, and interferometry: Photon gear, Dec. 2020. [Online]. Available: <https://photongear.com/>
- [55] M. Acton, K.-A. Brickman, P. Haljan, P. Lee, L. Deslauriers, and C. Monroe, "Near-perfect simultaneous measurement of a qubit register," *Quantum Inf. Comput.*, vol. 6, pp. 465–482, 2006, doi: [10.26421/QIC6.6](https://doi.org/10.26421/QIC6.6).
- [56] D. Lobser *et al.*, "JaqlPaw: A Guide to Defining Pulses and Waveforms for Jaql," Accessed: Jun. 2021. [Online]. Available: [https://www.sandia.gov/quantum/Projects/Uploads/JaqlPaw\\_\\_A\\_Guide\\_to\\_Defining\\_Pulses\\_and\\_Waveforms\\_for\\_Jaql.pdf](https://www.sandia.gov/quantum/Projects/Uploads/JaqlPaw__A_Guide_to_Defining_Pulses_and_Waveforms_for_Jaql.pdf)
- [57] R. Bowler, "Coherent ion transport in a multi-electrode trap array," Ph.D. dissertation, Dept. Phys., Univ. Colorado, Denver, CO, USA, 2015.
- [58] E. Mount *et al.*, "Scalable digital hardware for a trapped ion quantum computer," *Quantum Inf. Process.*, vol. 15, pp. 5281–5298, 2016, doi: [10.1007/s11128-015-1120-z](https://doi.org/10.1007/s11128-015-1120-z).
- [59] I. V. Inlek, G. Vittorini, D. Hucul, C. Crocker, and C. Monroe, "Quantum gates with phase stability over space and time," *Phys. Rev. A*, vol. 90, Oct. 2014, Art. no. 042316, doi: [10.1103/PhysRevA.90.042316](https://doi.org/10.1103/PhysRevA.90.042316).
- [60] E. Nielsen, J. K. Gamble, K. Rudinger, T. Scholten, K. Young, and R. Blume-Kohout, "Gate set tomography," 2020, *arXiv:2009.07301*.
- [61] H. Häffner, C. F. Roos, and R. Blatt, "Quantum computing with trapped ions," *Phys. Rep.*, vol. 469, pp. 155–203, Sep. 2008, doi: [10.1016/j.physrep.2008.09.003](https://doi.org/10.1016/j.physrep.2008.09.003).
- [62] Microchip, CsIII Model 4310B, Mar. 2021. [Online]. Available: <https://www.microsemi.com/product-directory/cesium-frequency-references/4114-csiii-model-4310b>
- [63] Microchip, Quartz ultra clean-up oscillator, Mar. 2021. [Online]. Available: <https://www.microsemi.com/existing-parts/part/138085>
- [64] Stanford Magnets, How Does Temperature Affect Samarium Cobalt Magnets, Mar. 2021. [Online]. Available: <https://www.stanfordmagnets.com/how-does-temperature-affect-samarium-cobalt-magnets.html>
- [65] E. L. Hahn, "Spin echos," *Phys. Rev.*, vol. 80, 1950, Art. no. 580, doi: [10.1103/PhysRev.80.580](https://doi.org/10.1103/PhysRev.80.580).
- [66] N. F. Ramsey, "A new molecular beam resonance method," *Phys. Rev.*, vol. 76, 1949, Art. no. 996, doi: [10.1103/PhysRev.76.996](https://doi.org/10.1103/PhysRev.76.996).
- [67] R. Blume-Kohout *et al.*, "Demonstration of qubit operations below a rigorous fault tolerance threshold with gate set tomography," *Nature Commun.*, vol. 8, 2017, Art. no. 14485, doi: [10.1038/ncomms14485](https://doi.org/10.1038/ncomms14485).
- [68] C. M. Shappert *et al.*, "Spatially uniform single-qubit gate operations with near-field microwaves and composite pulse compensation," *New J. Phys.*, vol. 15, 2013, Art. no. 083053, doi: [10.1088/1367-2630/15/8/083053](https://doi.org/10.1088/1367-2630/15/8/083053).
- [69] S. Wimperis, "Broadband, narrowband, and passband composite pulses for use in Advanced NMR Experiments," *J. Magn. Reson.*, vol. 109, no. 2, pp. 221–231, Jan. 1994, doi: [10.1006/jmra.1994.1159](https://doi.org/10.1006/jmra.1994.1159).
- [70] C. A. Sackett *et al.*, "Experimental entanglement of four particles," *Nature*, vol. 404, pp. 256–259, 2000, doi: [10.1038/35005011](https://doi.org/10.1038/35005011).
- [71] C. F. Roos, "Controlling the quantum state of trapped ions," Ph.D. dissertation, Inst. Exp. Phys., Univ. Innsbruck, Innsbruck, Austria, 2000.
- [72] U. Tanaka, K. Masuda, Y. Akimoto, K. Koda, Y. Ibaraki, and S. Urabe, "Micromotion compensation in a surface electrode trap by parametric excitation of trapped ions," *Appl. Phys. B*, vol. 107, pp. 907–912, Jun. 2011, doi: [10.1007/s00340-011-4762-2](https://doi.org/10.1007/s00340-011-4762-2).
- [73] S. Narayanan *et al.*, "Electric field compensation and sensing with a single ion in a planar trap," *J. Appl. Phys.*, vol. 110, 2011, Art. no. 114909, doi: [10.1063/1.3665647](https://doi.org/10.1063/1.3665647).



**Susan M. Clark** was born in Alexandria, VA, USA, in 1982. She received the B.S. degree in physics from Duke University, Durham, NC, USA, in 2004, and the Ph.D. degree in applied physics from Stanford University, Stanford, CA, USA, in 2010.

From 2010 to 2013, she was a Joint Quantum Institute Postdoctoral Fellow with the University of Maryland, College Park, MD, USA. At that time, she worked with Christopher Monroe demonstrating protocols for combining remote and local entanglement for scalable trapped-ion quantum systems. In 2013, she joined Sandia National Laboratories, Albuquerque, NM, USA, where she is currently a Principal Member of the Technical Staff. Since joining Sandia, she has worked on a variety of quantum information related projects involving trapped ions and gate defined quantum dots in Silicon.

Dr. Clark is currently the Principal Investigator of the Department of Energy Office of Science Advanced Scientific Computing Research funded program “Quantum Scientific Computing Open User Testbed.”



**Daniel Lobser** received the B.S. and Ph.D. degrees in physics from the University of Colorado, Boulder, CO, USA, in 2009 and 2015, respectively.

In 2015, he joined Sandia National Laboratories, Albuquerque, NM, USA, as a Postdoctoral Appointee and was converted to a Senior Member of the Technical Staff in 2017 and a Principal Member of Technical Staff in 2021. His research interests include the development of classical and quantum control systems for trapped-ion qubits.



**Melissa C. Revelle** received the B.S. degrees in physics and astronomy from the University of Arizona, Tucson, AZ, USA, in 2009, and the M.S. degree in physics and the Ph.D. degree in atomic physics from Rice University, Houston, TX, USA, in 2013 and 2016, respectively.

She is currently a Senior Member of Technical Staff with Sandia National Laboratories, Albuquerque, NM, USA. She was a Research Assistant studying the polarizability of atoms from 2007 to 2009 with the University of Arizona and investigating the dimensional crossover in ultracold Fermi gases from 2009 to 2016 with Rice University. Her research interests include coherent manipulation and control of trapped ions in microfabricated surface traps.

Dr. Revelle was the recipient of the Wilson Research Award from Rice University in 2017.



**Christopher G. Yale** received the B.S. degree in physics from Yale University, New Haven, CT, USA, in 2009, and the Ph.D. degree in physics from the University of California, Santa Barbara, CA, USA, in 2015.

From 2013 to 2016, he was a Visiting Graduate Student and later a Postdoctoral Scholar with the Institute for Molecular Engineering, University of Chicago, Chicago, IL, USA. He was then a Postdoctoral Appointee with the Sandia National Laboratories, Albuquerque, NM, USA, where he is currently a Senior Member of the Technical Staff. His research interests include trapped-ion quantum computing, solid-state quantum information processing, quantum optics, and photonics.

**David Bossert**, photograph and biography not available at the time of publication.

**Ashlyn D. Burch**, photograph and biography not available at the time of publication.

**Matthew N. Chow**, photograph and biography not available at the time of publication.

**Craig W. Hogle**, photograph and biography not available at the time of publication.

**Megan Ivory**, photograph and biography not available at the time of publication.

**Jessica Pehr**, photograph and biography not available at the time of publication.

**Bradley Salzbrenner**, photograph and biography not available at the time of publication.

**Daniel Stick**, photograph and biography not available at the time of publication.

**William Sweatt**, photograph and biography not available at the time of publication.

**Joshua M. Wilson**, photograph and biography not available at the time of publication.

**Edward Winrow**, photograph and biography not available at the time of publication.

**Peter Maunz**, photograph and biography not available at the time of publication.